SAMARIUM-BASED INTERMEDIATE TEMPERATURE SOLID OXIDE FUEL CELLS

A Thesis
Presented to
The Graduate Faculty of the University of Akron

In Partial Fulfillment
of the Requirements for the Degree
Master of Science

Felipe Guzman Montanez
December, 2005

SAMARIUM-BASED INTERMEDIATE TEMPERATURE SOLID OXIDE FUEL CELLS

Felipe Guzman Montanez

Thesis

Approved:	Accepted:
Advisor Dr. Steven Chuang	Dean of the College Dr. George K. Haritos
Faculty Reader	Dean of the Graduate School Dr. George R. Newkome
Faculty Reader	Date
Department Chair Dr. Lu-Kwang Ju	

ABSTRACT

The development of electrochemical converters (i.e. fuel cells) has attracted research interest during the last decades due to an increasing concern on the depletion of available fossil fuel reserves and environmental issues such as global warming and emission of pollutant gases. Solid oxide fuel cells have received special attention because of their higher energy efficiency, rapid electrode kinetics without using expensive electrocatalysts such as Pt, relative resistance to impurities in the fuel and the possibility of processing CO, CH_4 and other Carbon based fuels.

Extensive research efforts have resulted in the development of solid oxide fuel cell materials such as Yttria stabilized Zirconia (YSZ) electrolytes, Lanthanum or Calcium doped Strontium Manganite (LSM) cathodes and Ni-YSZ cermet anodes. YSZ electrolytes require high operation temperatures (~ 1000 °C) in order to achieve sufficient ionic conductivity, placing large restrictions to candidate electrode, interconnect and housing materials. As a result, the cost of solid oxide fuel cell systems has become an important factor preventing their commercialization.

Recent research efforts have shown that a variety of samarium doped oxides can be used as electrolyte and electrode materials in order to develop solid oxide fuel cells operating in intermediate temperatures. Samarium doped Ceria (SDC) has been shown to possess sufficient ionic conductivity at intermediate temperatures (600-800 °C).

Similarly, Strontium doped Samarium Cobaltite (SSC) has been shown to act as an active electrode material.

During this study we developed a synthesis procedure in order to fabricate a samarium doped ceria electrolyte and a samarium strontium cobaltite electrode material. Different fabrication conditions were tested in order to elucidate a procedure to manufacture an intermediate temperature fuel cell using an SDC electrolyte and two SSC electrodes. The impact of several fabrication variables on the resulting fuel cell performance was evaluated.

Results from this study concluded that SDC electrolyte materials can be successfully synthesized according to the pechini method. Similarly, SSC electrodes can be synthesized using a solid state reaction starting with respective oxide species. Fabrication of electrolyte supported fuel cells using an SDC electrolyte and two SSC were also developed according to a cold pressing technique. The effect of the solid electrolyte fabrication procedure on the fuel cell performance was also evaluated.

ACKNOWLEDGEMENTS

I wish to express my sincere gratitude to my research advisor professor Steven S.C Chuang for his continuous guidance and encouragement during the course of my research. I want to thank the Ohio Coal Development Office and Mr Bob Brown for their support. I would also like to thank Professor Lu-Kwang Ju and professor Gorge Chase for agreeing to serve on my committee.

I would also like to thank Camila for her constant support during these years, my colleagues Zhiqiang Yu, Rahul, Duane, and Jim for his friendship and pleasant working environment, Tom Quick from the Geology Department at The University of Akron for XRD characterization, and Mr Frank Pelc for his numerous contributions with the design of fuel cell systems.

I would like to dedicate this work to my family, who has always supported my and guided me since I was born.

TABLE OF CONTENTS

Page

LIST OF TABLES

Table Page

LIST OF FIGURES

CHAPTER I

INTRODUCTION

1.1 Energy Outlook:

Recent studies on worldwide energy consumption have estimated a 50-65% increase in energy demand in the next decade based on a set of assumptions on future economic growth and international fossil fuel prices *(1)*. Developing countries are expected to account for the majority of this energy increment, particularly emerging Asian economies such as China and India, where the energy consumption is projected to grow at an average annual rate of 2.7 percent between 2001 and 2025 (*1*-*3*). Table 1.1 presents estimated world energy consumption.

Conventional energy resources based on fossil fuels (i.e. oil, natural gas, coal) are expected to meet these increasing energy demands assuming low fossil fuel prices, non competitive alternative fuels costs and no changes on current environmental policies (*4*).

Particularly, oil and natural gas are expected to account for the majority of the energy market on residential, commercial and industrial sectors as well as in transportation applications (*1*).

Table 1.1 World Energy Consumption.

	ENERGY CONSUMPTION (QUATRILLION BTU)				CARBON DIOXIDE EMISSIONS (MILLION METRIC TONS)			
REGION	1990	2001	2010	2025	1990	2001	2010	2025
Industrialized Countries	182.8	211.5	236.3	281.4	10,462	11,634	12,938	15,643
EE / FSU	76.3	53.3	59.0	75.6	4,902	3,148	3,347	4,313
Developing Countries	89.3	139.2	175.5	256.9	6,200	9,118	11,379	17,168
Asia	52.5	85.0	110.6	173.4	3,994	6,012	7,647	11,801
Middle east	13.1	20.8	25.0	34.1	846	1,299	1,566	2,110
Africa	9.3	12.4	14.6	21.5	656	843	971	1,413
Central and South America	14.4	20.9	25.4	36.9	703	964	1,194	1,845
Total World	348.4	403.9	470.8	622.9	21,563	23,899	27,715	37,124

IEA, “World Energy Outlook” (DOE/EIA-0484) 2004.

Projections on worldwide fossil fuel reserves have shown a decreasing tendency on hydrocarbon production leading to an eventual complete depletion (*5*). Also, studies on environmental issues related to global climate changes and the release of green house effect gases have pointed the necessity of more stringent emission control regulations (*6-8*). These factors have become the driving force for many debates focusing on the development of alternative energy sources as well as more efficient, environmental friendly energy transformation technologies.

During recent years a number of approaches related to alternative fuels, energy carriers and more efficient energy converters have been proposed. Among these, the development of a hydrogen based economy in which centralized power plants producing electricity are replaced by a network of H_2 delivery systems with on site electricity generation (i.e. fuel cells), has become one of the most discussed initiatives (*9-13*).

The hydrogen economy has generated both defenders as well as detractors due to technical difficulties associated to H_2 production and storage. The key issues include lack of available methods for producing H_2 feed stocks that meet the demand at competitive costs within stringent environmental regulations as well as development of efficient storage systems have been discussed (*14-18*).

Regardless of the feasibility of H_2 economy, the development of new energy conversion devices capable of achieving efficiencies greater than current technologies constitutes a new area subject of numerous research efforts (*19*).

1.2 Fuel Cells:

Electrochemical energy transformers (i.e. fuel cells) have attracted considerable research interest because of their higher energy efficiency when compared with other conventional energy conversion technologies (i.e. thermoelectric energy converters), their low pollutant emissions and their excellent flexibility with available fuel stocks.

Fuel cells are electrochemical devices that transform the free energy difference of chemical reactions, such as the reactions involved in combustion processes, directly into electricity (*20*). Therefore, they are not subject to the Carnot cycle limitation of thermal machines. Although fuel cells and batteries have similar components and characteristics, they differ from common batteries since the former can supply electricity uninterruptedly as long as the fuel and the oxidant are continuously fed. In contrast, in primary batteries the available electrical energy is determined by the amount of reactants stored within the battery.

Fuel cells can have been classified according different criteria (*21*) such as the type of operating fuel and oxidant, the use of external or internal reforming, and the specific electrolyte material. According to this last criterion, there are polymer electrolyte fuel cells (PEMFC), alkaline fuel cells (AFC), Phosphoric acid fuel cells (PAFC), sulfuric acid fuel cells (SAFC), molten carbonate fuel cells (MCFC) and solid oxide fuel cells (SOFC). The first four types of fuel cells have in common their low to medium temperature of operation (80–650ºC) whereas the last two types of cells are characterized by their higher temperature operation (650-1000 ºC).

The structure of fuel cells is composed of an anode and a cathode electrode separated by an ion conducting electrolyte and connected only through a load by a metallic external circuit. The external circuit transports electric current whereas the electrolyte transports ions. Under operation conditions, the fuel is supplied continuously to the anode (negative electrode), and an oxidant is fed to the cathode (positive electrode). The anode electrode promotes one half cell reaction yielding electrons, which are transferred trough the external circuit to the cathode reactant. To complete the circuit, the second half reaction takes place on the cathode electrode and ions are transported trough the electrolyte from one electrode to the other. Figure 1.1 shows a schematic representation of a fuel cell operating with hydrogen as the fuel and oxygen as oxidant.

1.3 Solid Oxide Fuel cells

SOFCs have attracted considerable research interest because of its higher energy efficiency, rapid electrode kinetics without using expensive electrocatalysts such as Pt, relative resistance to impurities in the fuel, the possibility of processing CO, CH_4 and other Carbon based fuels, and flexibility to stacks of cells using interconnect materials generating robust power generation units (*21*).

SOFC are multilayer ceramic structures consisting of an ion conducting solid electrolyte connected to an anode and a cathode electrode.

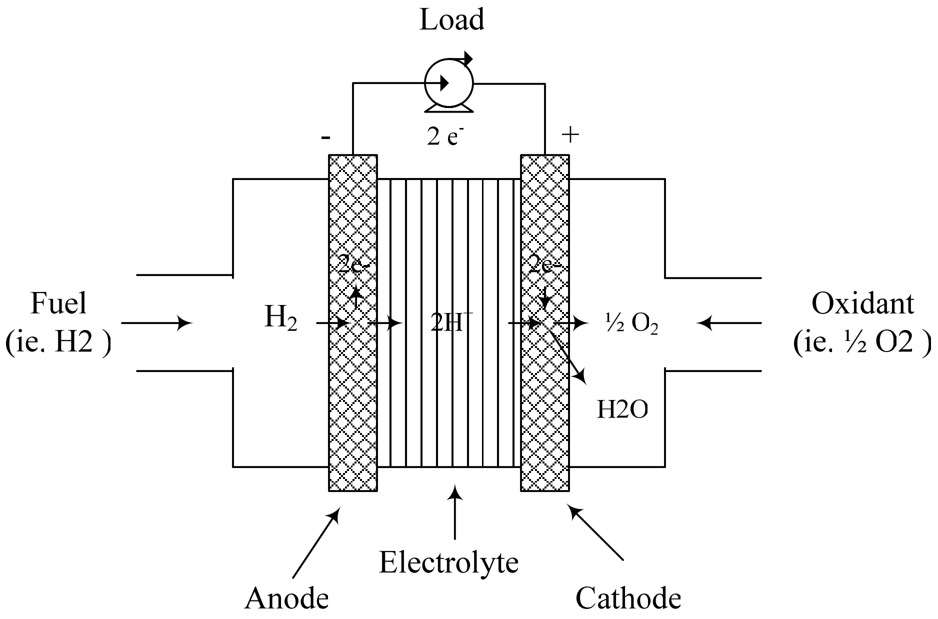

Anode reaction: $H_2 \longrightarrow 2H^+ + 2e^-$

Cathode reaction: $O_2 + 4H^+ + 4e^- \longrightarrow 2\,H_2O$

Overall reaction: $2H_2 + O_2 \longrightarrow 2\,H_2O$

Figure 1.1 Scheme of a fuel Cell.

During operation conditions, oxygen is dissociated at the cathode electrode forming oxygen ions (O^{-2}). These ions diffuse trough the electrolyte material to the anode side, where they react with the fuel forming the oxidation byproducts, and release electrons to the external circuit.

Conventional SOFC materials include Yttria Stabilized Zirconia (YSZ) solid electrolytes, Lanthanum or Calcium doped Strontium Manganite (LSM) cathodes electrode and a Ni-YSZ anode electrodes (*22*). YSZ electrolytes have been extensively investigated because of their high mechanical and chemical stability under the oxidizing and reducing conditions, low electronic conductivity, and relative low cost. However, YSZ based fuel cells require high operation temperature (~1000 ºC) in order to achieve sufficient ion conductivity.

High operation temperature places many restrictions on the selection of compatible electrode, interconnect and housing materials resulting in complicated fabrication procedures, elevated fuel cell manufacture costs, and reduce durability (*23*). Therefore the development of Intermediate Temperature Solid Oxide Fuel Cells (IT-SOFCs) that combine the rapid electrode kinetics and higher efficiencies of solid oxide fuel cells with an intermediate operating temperature (i.e. 600-800 ºC) would reduce fabrication costs making fuel cell technology an attractive approach for alternative energy transformation devices. To achieve this goal, research efforts have been directed towards the development of electrolyte materials having higher ionic conductivities at moderate temperatures and new electrodes exhibiting high catalytic activity and stability with respect to other fuel cell components (*24*, *25*).

Rare earth doped ceria materials have been identified as intermediate temperature electrolytes having much higher ion conductivities compared to YSZ. Among these, Samarium Doped Ceria (SDC) has received special attention due to its promising higher performance at temperature between 500 and 700 °C (*24, 26, 27*). SDC based SOFCs require the introduction of alternative electrode materials exhibiting high catalytic activity for electrochemical reactions, as well as compatibility with the electrolyte.

Perovskite-type oxides have received much attention due to their high electrical conductivity, and stability. Among these, Strontium doped Samarium Cobaltite (SSC) possess great compatibility with samarium doped electrolytes, making it a potential candidate for the development of electrode materials.

1.4 Objectives

The first objective of this study is to develop an experimental technique for the fabrication of intermediate temperature solid oxide fuel cells (IT-SOFC) based on a samarium doped ceria electrolyte and samarium strontium cobaltite cathode material. The effect of several ceramic processing variables on the properties of the major fuel cell components will be analyzed by means of different characterization techniques such as X-Ray diffraction, Raman spectroscopy and microscopy techniques.

The second objective of this study consists on evaluating the operation conditions leading to optimum power densities of the fabricated fuel cells. Measurements of cell voltage and current density will be analyzed using a Labview ^{TM} software.

1.5 Outline.

The structure of this thesis is outlined. Chapter I present an introduction on intermediate solid oxide fuel cells as well as the objectives and scope of this thesis. Chapter II provides limited background information on intermediate temperature solid oxide fuel cells including requirements for electrolyte and electrode materials, fuel cell architectures, and ceramic materials processing techniques. Chapter III contains a summary of the experimental techniques used in order to synthesize SDC electrolyte and SSC electrode materials, as well as the procedures used to fabricate electrolyte supported fuel cells. Chapter IV presents a limited discussion on the characterization of the synthesized fuel cell materials as well as on the effect of different variables during the fuel cell fabrication process. Chapter V provides a discussion on the performance of the manufactured fuel cells under different operation conditions and their relation to the fabrication procedures. Chapter VI contains a summary of results and significance.

CHAPTER II

BACKGROUND

The selection of materials for SOFC applications is rather limited due to the high operation temperature and the contact with a strong oxidizing and reducing environment at the anode and cathode electrode respectively. Therefore only a reduced number of materials meeting the requirements for a long term efficient operation have been developed (*1*).

Elevated temperatures create many difficulties including densification of electrodes, (decreasing the electrode porosity, and thus reducing the availability of surface area for reaction), formation of an insulating layer at the electrode electrolyte layer (affecting the ion transport process), crack formation due to large differences in thermal expansion coefficients among the different materials, and degradation of the fuel cell components during long term operation (*2*).

A reduction of the operation temperature (600-800 °C) constitutes an alternative to alleviate these problems, allowing a broader selection of materials for fuel cell components. However, intermediate operation temperatures place higher performance requirements on fuel cell components, including the anode and cathode electrodes, as well as the electrolyte

Therefore the fabrication of IT-SOFCs requires the development of high ion conductive electrolytes as well as electrodes that encompass high catalytic activity, mechanical stability under the reaction atmospheres, and compatible thermal expansion coefficients at the operation temperature.

2.1 Electrolyte materials.

Development of high performance solid electrolytes for IT-SOFCs involves selecting materials that meet numerous requirements such as high ionic conductivity, negligible electronic conductivity, small gas permeability, and chemical stability over a wide range of oxygen partial pressures. Mechanical properties such as toughness are also desired characteristics, especially for mobile applications. Additionally, electrolyte materials must be abundant and must have relatively low production and manufacture costs (*3*, *4*). Selection of candidate materials requires careful evaluation of each of the enumerated properties. However, estimation of ionic conductivities, ionic and electronic domains, and thermal expansion coefficients are usually the first aspects to be examined.

2.1.1 Electrolyte ion conductivity

The presence of ionic conductivity in solid oxides is closely related to the crystalline structure as well as to the composition of the material. Therefore, detailed characterization of the electrolyte phase and chemical composition is required for the successful development of high performance electrolytes.

The majority of the materials that have been found useful as solid electrolytes can be classified according to their structure as fluorite or perovskite structured materials (*5*). Electrolytes having fluorite structure consists of face centered cubic arrangement of cations with anions located at tetrahedral sites, resulting in a large number of interstitial voids. Addition of divalent or trivalent cations such as alkaline earth oxides or rare earth oxides generates oxygen vacancies in order to maintain electro-neutrality, leading to development of ionic conductivity. The magnitude of the ion conductivity strongly depends on the properties of the doping cation as well as on its concentration, which is limited by the solid solubility of the oxide system. The highest ionic conductivity is usually achieved when the minimum amount of dopant for stabilizing the fluorite structure is introduced. Examples of fluorite structured solid electrolytes include Zirconia based (ZrO_2), Ceria based (CeO_2), Bismuth oxide (Bi_2O_3) and Thorium based (ThO_2) oxides.

Materials having perovskite structure have a great potential for developing electrolytes as well as anode and cathode electrodes for SOFC applications. Perovskite oxides respond to the general formula ABO_3 where A is a large cation with coordination number of 12 and B is a small cation with coordination number 6. These materials can accommodate a large number of oxygen vacancies, resulting in high ionic conductivity. First row transition metals capable of exhibiting multiple valences under different conditions can occupy the small B sites, leading to enhanced electron conductivity. In addition, several derivative structures such as brownmillerite (derived from $Ba_2In_2O_5$) and orthoferrite exhibiting unique transport properties can be obtained. Examples of perovskite electrolytes include $LaGaO_3$ based oxides (*6*).

Recent studies have lead to the discovery of newer crystalline phases exhibiting ion conductivity. Among these, the apatite-type structure has attracted several research efforts (*7*). The apatite phase responds to the general formula $A_{10-x}(MO_4)_6O_{2\pm\delta}$ where M=Si or Ge and A corresponds to rare earth and alkaline cations (*4*). Table 2.1 presents typical ionic conductivities for selected fluorite, perovskite, and apatite structured electrolyte materials.

2.1.2 Solid electrolyte conductivity domain.

Appearance of ionic conductivity in solid oxide systems can be accompanied by the presence of electronic conductivity (i.e. mixed ionic-electronic conductors), therefore, total conductivity is commonly expressed as the sum of the electronic conductivity contribution σ_e, and the ionic conductivity contribution σ_i .

$$\sigma = \sigma_e + \sigma_i \qquad \text{(Eq 2.1)}$$

The specific contribution of ionic and electronic conductivity for a given solid electrolyte material strongly depends on temperature, oxygen chemical potential, as well as dopant concentration. Investigations on the specific relations between conductivity, oxygen chemical potential and temperatures have been conducted for a number of solid electrolytes (*8-10*). High performance electrolyte materials require the presence of large ionic conductivity with negligible electronic conductivity over a wide range of oxygen chemical potentials covering the temperatures and oxygen potentials typically encountered during steady state operation and fuel cell cycling. As a result, careful evaluation of the electronic and ionic domain for candidate electrolyte materials must be taken into account. Electrolyte domains for selected electrolyte materials have been reported on literature sources (*4, 11*).

2.1.3 Thermal expansion coefficient

Candidates for high performance IT-SOFC electrolytes also require physical properties such as thermal expansion coefficients matching those of the complementary fuel cell components (i.e. anode, cathode interconnect and seal materials) in order to ensure long term operation, and strength during cycling. Table 2.2 present thermal expansion coefficients for selected electrolyte materials.

2.2 Ceria-based electrolyte materials for intermediate temperature fuel cells

During the last 15 years many research efforts have lead to the identification of several potential candidates for developing high performance electrolyte materials capable of operating at intermediate temperatures. However, only few of them have been found to meet the multiple requirements to serve as IT-SOFC electrolytes. The majority

Table 2.1. Ionic conductivity for selected electrolyte materials.

Composition	**Structure**	**Temperature (°C)**	**Ionic Conductivity (ohm^{-1} cm^{-1} x 10^{2})**	**Reference**
8% - YSZ $(ZrO_2)_{0.92}(Y_2O_3)_{0.08}$	Fluorite	600	0.5	(*12*, *13*)
		700	1.3	
		800	2.9	
		900	5.8	
		1000	10.3	
10% - YSZ $(ZrO_2)_{0.90}(Y_2O_3)_{0.10}$	Fluorite	600	0.2	(*12*)
		700	0.7	
		800	1.7	
		900	3.6	
		1000	8.3	
15% - YSZ $(ZrO_2)_{0.85}(Y_2O_3)_{0.15}$	Fluorite	600	0.08	(*12*)
		700	0.25	
		800	0.7	
		900	2	
		1000	3.6	

Table 2.1. Ionic conductivity for selected electrolyte materials continued.

Composition	**Structure**	**Temperature (°C)**	**Ionic Conductivity (ohm^{-1} cm^{-1} x 10^{2})**	**Reference**
12% - ZCO $(ZrO_2)_{0.88}(CaO)_{0.12}$	Fluorite	600 700 800 900	0.25 0.5 1.1 2.86	(*12*)
14% - ZCO $(ZrO2)_{0.86}(CaO)_{0.14}$	Fluorite	600 700 800 1000	0.09 0.17 0.5 1.7	(*12*)
6% - ZYbO $(ZrO2)_{0.94}(Yb_2O_3)_{0.06}$	Fluorite	600 700 800 900	0.1 0.3 0.8 1.8	(*13*)
8% - ZYbO $(ZrO2)_{0.92}(Yb_2O_3)_{0.08}$	Fluorite	600 700 800 900	0.38 1 2.5 4.9	(*13*)

Table 2.1. Ionic conductivity for selected electrolyte materials continued.

Composition	**Structure**	**Temperature (°C)**	**Ionic Conductivity (ohm^{-1} cm^{-1} x 10^2)**	**Reference**
9% - ZYbO $(ZrO2)_{0.91}(Yb_2O_3)_{0.09}$	Fluorite	600 700 800 900	0.1 1 2.5 10	(*12*)
10% - ZYbO $(ZrO2)_{0.90}(Yb_2O_3)_{0.10}$	Fluorite	600 700 800 900	0.32 1 2.7 5.8	(*13*)
12% - ZYbO $(ZrO2)_{0.88}(Yb_2O_3)_{0.12}$	Fluorite	600 700 800 900	0.18 0.7 1.8 4.3	(*13*)
15% - ZYbO $(ZrO2)_{0.85}(Yb2O3)_{0.15}$	Fluorite	600 700 800 900	N / A 0.08 0.17 7.1	(*12*)

Table 2.1. Ionic conductivity for selected electrolyte materials continued.

Composition	**Structure**	**Temperature (°C)**	**Ionic Conductivity (ohm^{-1} cm^{-1} x 10^2)**	**Reference**
6% - ZSO $(ZrO2)_{0.94}(Sc_2O_3)_{0.06}$	Fluorite	600 700 800 900	0.57 1.7 3.6 7.0	(*13*)
8% - ZSO $(ZrO2)_{0.92}(Sc_2O_3)_{0.08}$	Fluorite	600 700 800 900	1.6 3.9 8.2 15	(*13*)
10% - ZSO $(ZrO2)_{0.90}(Sc_2O_3)_{0.10}$	Fluorite	600 700 800 900	1.7 4.1 8.4 15.3	(*13*)
12% - ZSO $(ZrO2)_{0.88}(Sc_2O_3)_{0.12}$	Fluorite	600 700 800 900	0.8 2.3 5.4 11	(*13*)

Table 2.1. Ionic conductivity for selected electrolyte materials continued.

Composition	**Structure**	**Temperature (°C)**	**Ionic Conductivity (ohm^{-1} cm^{-1} x 10^2)**	**Reference**
15% - ZSO $(ZrO2)_{0.85}(Sc_2O_3)_{0.15}$	Fluorite	600	N /A	(*12*)
		700	0.09	
		800	0.7	
		900	5	
$(ZrO_2)_{0.85}$ $(Nd_2O_3)_{0.15}$	Fluorite	600	0.01	(*12*)
		700	0.05	
		800	0.1	
		900	0.25	
$(ZrO_2)_{0.94}$ $(Sm_2O_3)_{0.06}$	Fluorite	600	0.09	(*13*)
		700	0.30	
		800	0.80	
		900	1.80	
$(ZrO_2)_{0.92}$ $(Sm_2O_3)_{0.08}$	Fluorite	600	0.03	(*13*)
		700	0.11	
		800	0.34	
		900	0.86	

Table 2.1. Ionic conductivity for selected electrolyte materials continued.

Composition	**Structure**	**Temperature (°C)**	**Ionic Conductivity (ohm^{-1} cm^{-1} x 10^{2})**	**Reference**
$(ZrO_2)_{0.90}$ $(Sm_2O_3)_{0.10}$	Fluorite	600 700 800 900	0.10 0.4 1.1 2.7	(*13*)
$(ZrO_2)_{0.88}$ $(Sm_2O_3)_{0.12}$	Fluorite	600 700 800 900	<0.0001 0.002 0.006 0.01	(*13*)
$(ThO_2)_{0.94}$ $(Y_2O_3)_{0.06}$	--	800 900 1000	0.06 0.2 0.4	(*8*)
$(ThO_2)_{0.85}$ $(Y_2O_3)_{0.15}$	--	800 900 1000	0.15 0.37 0.75	(*8*)

Table 2.1. Ionic conductivity for selected electrolyte materials continued.

Composition	**Structure**	**Temperature (°C)**	**Ionic Conductivity (ohm^{-1} cm^{-1} x 10^{2})**	**Reference**
$(ThO_2)_{0.85} (Y_2O_3)_{0.15}$	--	800 900 1000	0.15 0.37 0.75	(*8*)
$(ThO_2)_{0.75} (Y_2O_3)_{0.25}$	--	800 900 1000	0.09 0.2 0.6	(*8*)
$(ThO_2)_{0.88} (CaO)_{0.12}$	--	800 900 1000	0.07 0.23 0.4	(*14*)
$(ThO_2)_{0.8} (CaO)_{0.2}$	--	800 900 1000	0.002 0.063 0.1	(*14*)
$(ThO_2)_{0.7} (CaO)_{0.3}$	--	800 900 1000	<0.001 0.04 0.07	(*14*)

Table 2.1. Ionic conductivity for selected electrolyte materials continued.

Composition	**Structure**	**Temperature (°C)**	**Ionic Conductivity (ohm^{-1} cm^{-1} x 10^{2})**	**Reference**
$(BiO_2O_3)_{0.75}(Y_2O_3)_{0.25}$	Fcc	500	1	(*15*-*17*)
		600	8.5	
		700	18	
		800	50	
$(BiO_2O_3)_{0.8}$ $(SrO)_{0.2}$	Rhb	500	0.6	(*18*)
		600	2.5	
		700	22	
$(BiO_2O_3)_{0.9}(La_2O_3)_{0.1}$	Fcc	500	8.25	(*18*)
		600	10	
		700	N/A	
$(BiO_2O_3)_{0.7}(La_2O_3)_{0.3}$	Fcc	500	2	(*18*)
		600	6	
$(BiO_2O_3)_{0.8}(CaO)_{0.2}$	Fcc	500	2	(*18*)
		600	15	
$(BiO_2O_3)_{0.6}(CaO)_{0.4}$	Fcc	500	1	(*18*)
		600	1	

Table 2.1. Ionic conductivity for selected electrolyte materials continued.

Composition	**Structure**	**Temperature (°C)**	**Ionic Conductivity (ohm^{-1} cm^{-1} x 10^{2})**	**Reference**
$(BiO_2O_3)_{0.78}(WO_3)_{0.22}$	Fcc	500 600 700	2.5 6.3 12.6	(*19*)
BICUVOX.10 ($Bi_2V_{1.9}Cu_{0.1}O_{5.35}$)	Apatite	500 600 800	6.3 10 25.1	(*20*, *21*)
LSGM ($La_{0.9}Sr_{0.1}Ga_{0.8}Mg_{0.2}O_{2.85}$)	Perovskite	500 600 800	9 40 98	(*20*, *22*)
LSMO ($La_{0.5}Sr_{0.5}MnO_3$)		800	5.9 x 10-6	(*23*)
(CeO_2)	Fluorite	700 800 900	0.002 0.02 0.1	(*11*, *24*, *25*)

Table 2.1. Ionic conductivity for selected electrolyte materials continued.

Composition	**Structure**	**Temperature (°C)**	**Ionic Conductivity (ohm^{-1} cm^{-1} x 10^{2})**	**Reference**
$(CeO_2)_{0.9}(CaO)_{0.1}$	Fluorite	600	2.1	(*11*, *24*)
		700	4.5	
		800	9.9	
		900	22.2	
$(CeO_2)_{0.7}(CaO)_{0.3}$	Fluorite	600	1.9	(*11*, *24*)
		700	3.6	
		800	6.3	
		900	14	
$(CeO_2)_{0.9}(SrO)_{0.1}$	Fluorite	600	1.9	(*11*, *24*)
		700	2.9	
		800	5.0	
		900	14	
$(CeO_2)_{0.7}(SrO)_{0.3}$	Fluorite	600	0.4	(*11*, *24*)
		700	0.7	
		800	1.4	
		900	2.5	

Table 2.1. Ionic conductivity for selected electrolyte materials continued.

Composition	**Structure**	**Temperature (°C)**	**Ionic Conductivity (ohm^{-1} cm^{-1} x 10^{2})**	**Reference**
$(CeO_2)_{0.9}(BaO)_{0.1}$	Fluorite	600 700 800 900	0.03 0.05 0.1 0.2	(*11*, *24*)
$(CeO_2)_{0.9}(MgO)_{0.1}$	Fluorite	600 700 800 900	0.01 0.04 0.13 0.28	(*11*, *24*)
$(CeO_2)_{0.8}(Sm_2O_3)_{0.2}$	Fluorite	600 700 800 900	1.4 4.9 9.3 14.5	(*11*, *25*)

Table 2.1. Ionic conductivity for selected electrolyte materials continued.

Composition	Structure	Temperature (°C)	Ionic Conductivity (ohm^{-1} cm^{-1} x 10^2)	Reference
$(CeO_2)_{0.8}(Gd_2O_3)_{0.2}$	Fluorite	600 700 800 900	0.4 2.1 1.5 12.3	(*11*, *25*)
$(CeO_2)_{0.8}(Y_2O_3)_{0.2}$	Fluorite	600 700 800 900	0.4 1.5 2.9 6.8	(*11*, *25*, *26*)
$(CeO_2)_{0.8}(CaO)_{0.2}$	Fluorite	600 700 800 900	0.7 2.6 4.7 9.6	(*11*, *25*-*27*)
$(CeO_2)_{0.8}(La_2O_3)_{0.2}$	Fluorite	600 700 800 900	0.3 0.6 1.8 4.0	(*28*)

of currently accepted electrolytes can be classified as lanthanum gallate based electrolytes, ceria based electrolytes and bismuth based electrolytes.

Lanthanum gallate electrolytes possess several advantages including high ionic conductivity at intermediate temperature, a large electrolytic domain that extends down to very low oxygen potentials and relatively low thermal expansion coefficients (*29-31*). However, disadvantages such as reduction and volatilization of gallium oxide (MP = 1900°C), formation of secondary phases during the material processing, and relatively high cost of gallium limit their development.

Bismuth oxide-based electrolytes have been studied because of their higher ionic conductivity (*16, 36*); however, they are thermodynamically unstable when placed under reducing atmospheres and undergoes decomposition causing conductivity decrease (*16*). Introduction of protective coatings has been suggested as an alternative approach to overcome this problem.

Ceria-based electrolytes have attracted much attention because of their high ionic conductivity when compared to traditional zirconia based electrolytes (i.e. YSZ), good mechanical stability, and their lower cost compared to lanthanum gallate electrolytes. Therefore, they are considered very promising materials for the development of high performance electrolytes for IT-SOFC (*4*). Although ceria based electrolytes offer advantages in respect to other candidate electrolytes, one major drawback is the reduction of Ce^{+4} to Ce^{+3} when exposed to reducing conditions such as the ones often encounter at the anode side. Alternatives to alleviate this problem include special synthesis procedures, employment of protective layers, and introduction of co-dopants (*37, 38*).

Table 2.2 Thermal Expansion Coefficients for selected electrolyte materials

Electrolyte	**Thermal Expansion coefficient (α x 10^6 K^{-1})**	**Reference**
$(ZrO_2)_{0.92}$ $(Y_2O_3)_{0.08}$	10.4	(*4, 32*)
$(ZrO_2)_{0.91}$ $(Y_2O_3)_{0.09}$	9.5	(*4*)
$(ZrO_2)_{0.90}$ $(Y_2O_3)_{0.10}$	10.6	(*4*)
$(ZrO_2)_{0.92}$ $(Sc_2O_3)_{0.08}$	10.4	(*4*)
$(ZrO_2)_{0.90}$ $(Sc_2O_3)_{0.10}$	10.9	(*4*)
$(CeO_2)_{0.9}$ $(Gd_2O_3)_{0.1}$	12.4	(*4*)
$(CeO_2)_{0.8}$ $(Gd_2O_3)_{0.2}$	12.5	(*4*)
$(CeO_2)_{0.83}$ $(Sm_2O_3)_{0.17}$	8.6	(*33*)
$(CeO_2)_{0.8}$ $(Sm_2O_3)_{0.20}$	11.4	(*32*)
$(CeO_2)_{0.91}$ $(CaO)_{0.09}$	9.4	(*33*)
$La_{0.9}Sr_{0.1}Ga_{0.8}Mg_{0.2}O_{3-\delta}$	10.4	(*4*)
$La_{0.8}Sr_{0.2}Ga_{0.8}Mg_{0.2}O_{3-\delta}$	12.4	(*4*)
$La_{0.9}Sr_{0.1}Ga_{0.76}Mg_{0.19}Co_{0.05}O_{3-\delta}$	12.7	(*4*)
$La_{0.9}Sr_{0.1}Ga_{0.76}Mg_{0.19}Fe_{0.05}O_{3-\delta}$	11.7	(*4*)
$La_{0.9}Sr_{0.1}Ga_{0.45}Al_{0.45}Mg_{0.1}O_{3-\delta}$	10.9	(*4*)
$La_{9.83}Si_{4.5}AlFe_{0.5}O_{26-\delta}$	11.2	(*4*)

Table 2.2 Thermal Expansion Coefficients for selected electrolyte materials continued.

Electrolyte	**Thermal Expansion coefficient (α x 10^6 K^{-1})**	**Reference**
$La_7 Sr_3 Si_6 O_{24}$	8.9	(*4*)
$La_{1.7} Ca_{0.3} Mo_2 O_9$	17.85	(*34*)
$(Bi_2O_3)_{0.7}(Pr_2O_{11/3})_{0.09}$	15.3	(*35*)
$La_{1.7} Bi_{0.3} Mo_2 O_9$	16	(*4*)
$La_2 Mo_{1.7} W_{0.3} O_9$	14.4	(*4*)
$Bi_2 V_{0.9} Cu_{0.1} O_{5.5-\delta}$	15.3	(*4*)
$Ce_{0.8} Pr_{0.2} O_{2-\delta}$	11.9	(*34*)
$La_{1.7} Bi_{0.3} Mo_2 O_9$	15.6	(*34*)
$La_2 Mo_{1.7} W_{0.3} O_9$	17.1	(*34*)
$La_2 Mo_{1.95} V_{0.05} O_9$	18.65	(*34*)

2.2.1 Structure and ion conductivity of Ceria based electrolytes

Cerium oxide (CeO_2) has a fluorite structure forming a simple cubic packing of oxygen ions around a cerium Ce^{+4} central atom. The cerium atoms occupy half the octahedral sites provided by the oxygen ions, and the face- entered cubic packing of cerium ions forms a unit cell with a lattice parameter of 5.411 Å (*11*). Figure 2.1 shows a schematic representation of the ceria structure.

In contrast to other fluorite structures such as zirconium and hafnium oxides, pure CeO_2 does not exhibit phase transitions in oxidizing environments up to its melting point. Under such conditions, the amount of non stoichiometric O_2 in the CeO_2 structure is relatively small (*39*). As a result, few defects leading to oxygen vacancies are exhibited. Development of ionic conductivity is only achieved by introduction of divalent or trivalent cation impurities (i.e. dopants).

When rare earth dopant cations (i.e. M^{+2} or M^{+3}) are introduced in to the cerium oxide host structure as dopants, oxygen vacancies are generated in order to maintain electroneutrality, as it is described by the following defect reaction.

$$xMO_{1.5} + (1-x)CeO_2 \rightarrow xM'_{Ce} + 0.5xV_O^{\cdot\cdot} + (1-x)Ce_{Ce}^{x} + (2-0.5x)O_O^{x}$$

This reaction suggests that when x moles of $MO_{1.5}$ are introduced, the octahedral sites are filled with with x moles of dopant cation M^{+3} and (1-x) moles of host Ce^{+4}, and in the same way, O^{-2} ion sites are occupied by 0.5x moles of oxygen vacancies and (2-0.5x) moles of host O^{-2} ions. Figure 2.2 presents a schematic representation of the presence of oxygen vacancies on ceria structured electrolytes.

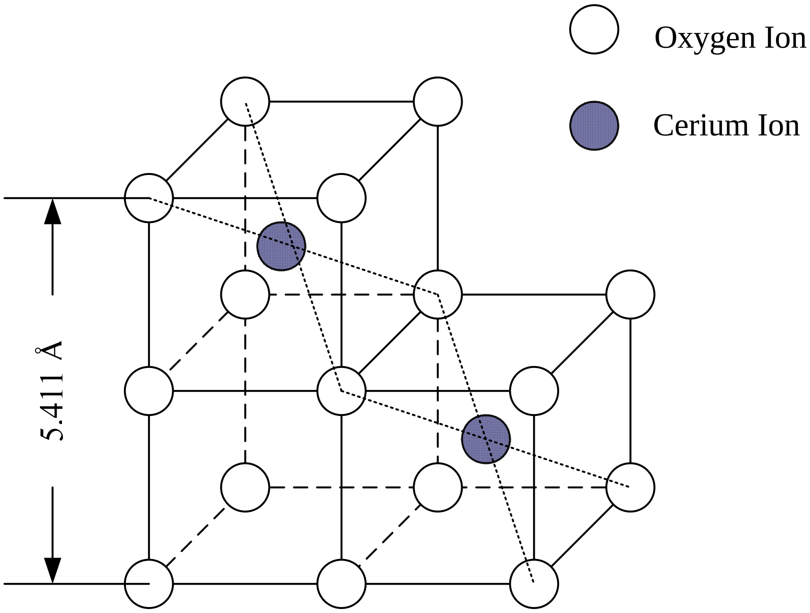

Figure 2.1 Unit cell of pure ceria (fluorite structure)

Different dopants can be introduced in the ceria structure in order to generate vacancies and thus, increase the oxygen ionic conductivity. The type and the composition of the dopant have a strong influence on the physical properties of the electrolyte. Research efforts have focused on studying the impact of selected ambivalent cation dopants such as gadolinium (Gd_2O_3), samarium (Sm_2O_3), erbium (Er_2O_3), and ytterbium (Yb_2O_3) oxides, on the exhibited ion conductivity for ceria based electrolytes. Among these ceria-based electrolyte systems, samarium doped ceria (SDC) and gadolinium doped ceria (GDC) have shown the highest ionic conductivities, making them the most attractive electrolytes for IT-SOFC applications (*4, 11*).

2.3 Samarium doped ceria (SDC) electrolytes

The conductivity exhibited by SDC electrolytes can be explained considering the theory of conductivity described in literature references (*11*). According to this theory, the electrical conductivity σ of doped fluorite oxides has been empirically written as

$$\sigma T = A \cdot \exp\left[\frac{-Ea}{kT}\right] \quad \text{(Eq 2.2)}$$

Where A is a pre exponential factor and Ea is the activation energy for conduction. The conductivity of ions can be expressed as the sum of the products of the concentration n_i, the mobility μ_i of charge carriers with charge q_i

$$\sigma = \sum_i n_i \cdot q_i \cdot \mu_i \quad \text{(Eq 2.3)}$$

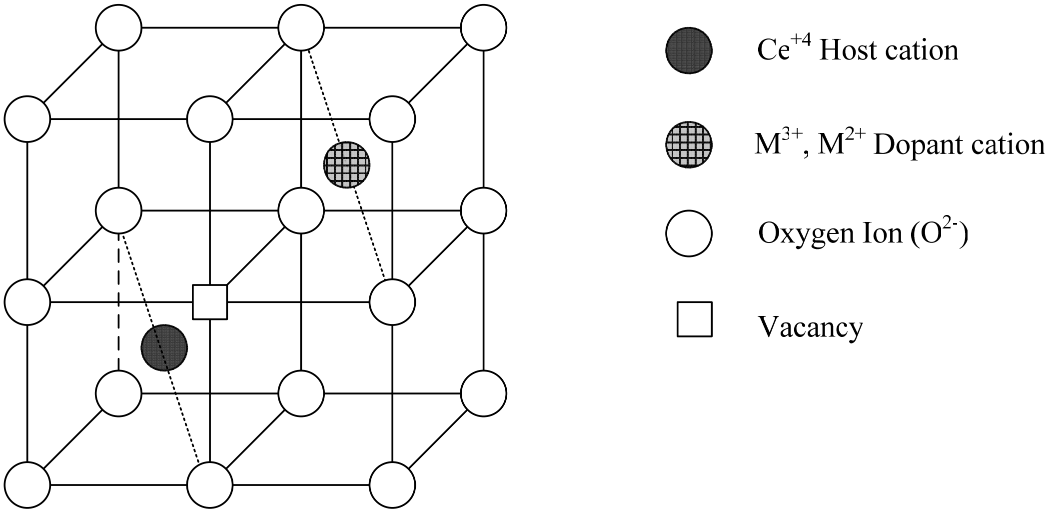

Figure 2.2 Half unit cell of the Ceria (Ce^{+4}) fluorite structure showing the position of dopant cation and oxygen vacancy.

In the case of oxygen ions the conductivity occurs via anions vacancies as expressed in equation 2.4.

$$\sigma_v = C_v \cdot q_v \cdot \mu_v \quad \text{(Eq 2.4)}$$

Where σ_v is the ion conductivity; q_v is the charge, μ_v is the mobility, and C_v is the concentration of oxygen vacancies. The mobility is related to the diffusivity D according to the Nernst-Einstein equation, where B represents the absolute mobility.

$$\mu_v = q_v \cdot B = \frac{q_v \cdot D}{kT} \quad \text{(Eq 2.5)}$$

The diffusivity D is usually expressed as an exponential function that relates a charge jumping distance between vacancies, an appropriate lattice vibration frequency ν_o and an activation enthalpy and entropy of diffusion ΔH_m, ΔS_m.

$$D = a^2 \upsilon_o \exp\left[\frac{\Delta S_m}{k}\right] \cdot \exp\left[\frac{-\Delta H_m}{kT}\right] \quad \text{(Eq 2.6)}$$

Additional considerations and simplifications allow the development of the following expression for the ionic conductivity of solid electrolytes.

$$\sigma T = A_1 \times \exp\left[\frac{-\Delta H_m}{kT}\right] \quad \text{(Eq 2.7)}$$

Were A_1 includes de entropy term as well as the vacancy concentration term. From this expression it can be concluding that small activation enthalpy leads to higher ionic conductivity. Different conductivity studies have concluded that smaller activation enthalpies are usually found when host and dopant ionic radii are very similar (*11*).

Among ceria solutions doped with rare earth oxides, Sm^{+3} has an ionic radius very similar to the Ce^{+4} ion (0.11 nm), leading to smaller association enthalpies and larger ionic conductivities when compared to other rare earth dopants.

Further theoretical analysis *(11)* has shown that the dependence of electrical conductivity of doped fluorite oxides with respect to temperature can not be expressed by a single exponential function. According to this theory, the temperature dependence can be shown as three regions. In region I, which appears at high temperatures, the electrical conduction is determined by the intrinsic defects in the crystal. In region II the conductivity is controlled by the population of charge carrying defect determined by an aliovalent dopant or impurity. In region III, usually at low temperatures, the population of charge carrying defects is determined by the thermodynamic equilibrium between the defects and the associated pairs.

The vacancies induced by doping aliovalent cations into the ceria structure are not free but bound to dopant cations to form defect associates. Therefore, description of the ion conductivity with respect to temperature requires detailed considerations on the defect association, as it has been presented by Kilner and Steel *(73)*. According to those authors, the defect association can be summarized in three major cases. In the first case, the dopant cation with valence 2 makes an associate with the oxygen vacancy and only one single defect associate is possible. In the second case, the dopant cation with the valence of 3 makes an associate with oxygen vacancy. In this case, the major defect is the associate of dopant and oxygen vacancy with one positive charge. Finally, the third case is that all the oxygen vacancies are free. Different expressions of the dependence of conductivity with respect to temperature can be derived based on each association defect case. Results have been summarized elsewhere *(73)*.

2.3.1 Effect of Samarium concentration on Ionic conductivity.

Ionic conductivity for ceria-based electrolytes has been shown to depend on the concentration of dopant cation, exhibiting a maximum point at a specific concentration, depending on the dopant under study. For SDC, 20 % mol dopant has been reported to achieve the highest ionic conductivity. Figure 2.3 presents the ionic conductivity of Samarium doped Ceria electrolytes for different dopant concentrations.

Theoretical models explaining this behavior introduce the concept of total activation energy for conduction Ea as the sum of the activation enthalpy (ΔH_m) and the association enthalpy ΔH_A.

$$E_a = \Delta H_m + \Delta H_A \quad (2.8)$$

According to this theory, the activation enthalpy (ΔH_m) is considered independent of dopant concentration, whereas the association enthalpy ΔH_A depends on the dopant concentration. Pre exponential factor also depends on dopant concentration, leading to a complex expression of conductivity respect to dopant concentration. Hence, dopant concentration for minimum association enthalpy usually does not match dopant concentration for ionic conductivity.

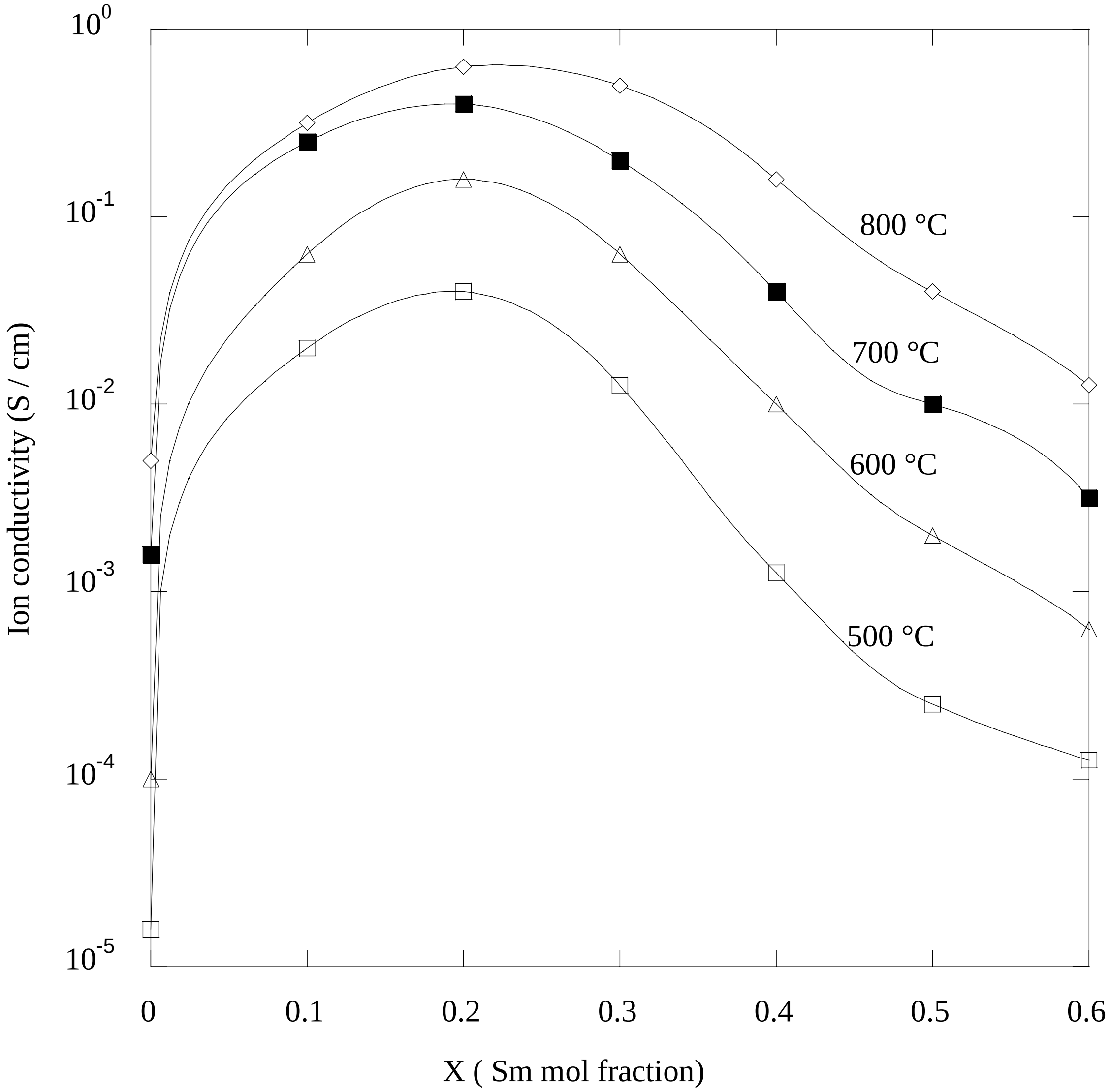

Figure 2.3 Ionic conductivity for x mol % Sm-SDC electrolytes at different temperatures.

2.3.2 SDC conductivity domain.

Although samarium doped ceria electrolytes have several advantages that make them candidates for IT-SOFC, there are also challenging difficulties that must be overcome in order to develop high performance fuel cell systems. The main disadvantage of SDC electrolytes is related to the development of significant n-type electronic conductivity due to the partial reduction of Ce^{+4} to Ce^{+3} at the low oxygen partial pressures experimented at the anode electrode. Several approaches have been proposed in order to suppress electronic conductivity on SDC electrolytes, including the selection of appropriate operation conditions, special fabrication procedures, and addition of protective coatings (*37, 38, 40, 41*).

2.4 Anode electrode materials

High performance anode electrodes must possess high electronic conductivity under strongly reducing conditions (low oxygen partial pressures), excellent catalytic activity for the electrochemical oxidation of the fuel, resistance to impurities present on the fuel, accessibility of a large number of reaction sites, high surface oxygen exchange kinetics, intimate contact with the electrolyte material and chemical and dimensional stability with the other fuel cell components in order to minimize thermal stress and formation of insulating layers. (*42, 43*). Candidate materials for anode electrodes include metallic cermets, and single phase oxides such as fluorite, rutile, and perovskite structured materials.

2.4.1 Metallic cermet anode materials

Metallic materials have electronic conductivity as well as catalytic activity for oxidation reactions. Therefore several noble and transition metals such as, Pt, Ni and Ru have been investigated in conventional fuel cell systems (*44-46*). Pure metals present difficulties due to thermal expansion coefficient mismatch, formation of aggregates during operation conditions (blocking the access of the fuel to the reaction sites), and interaction with oxidation products leading to corrosion issues (*44*). Thus, composite materials (cermets) having a metallic component embedded in a ceramic matrix, usually made of the electrolyte material, constitute the preferred alternative (*47*).

Nickel-based cermets have been identified as active anode materials for H_2 oxidation (*48*). However, when operating with carbon based fuels such as natural gas, Nickel-based electrodes exhibit large activity for internal reforming reactions, resulting in carbon deposition (*49*). Deposited carbon particles block the access to active sites causing loss of performance (*50, 51*). High steam/methane fuel mixtures have been used in order to suppress carbon deposition, however this approach results in lost of electrical efficiency (dilute fuel feed).

Cu-CeO_2 cermets have been explored as anode materials for direct oxidation of hydrocarbons under fuel cell operation resulting in negligible carbon deposition (*52-54*).

However due to their relatively low melting temperature (1085 °C) Cu tends to agglomerate during long term operation, leading to a loss in active sites and decrease in fuel cell performance. Alternatively, different formulations of Ni–Cu cermets have been reported to produce smaller carbon depositions when operating on hydrocarbon fuels (*55*).

2.4.2 Single phase oxide anode materials

Different single phase oxides having a defined structure such as fluorite, perovskite, and rutile have been investigated as possible anode materials. Among Fluorite materials, zirconia-based oxides doped with transition metals in order to introduce mixed conduction constitute an excellent alternative from the thermal expansion coefficient point of view. Although solid solutions of zirconia and several transition metals can be obtain, the resulting electronic conductivity under reducing environments is not high enough to meet the anode conductivity requirements (*42*). Rutile structured phases consists of a distorted hexagonal close packed anion structure in which octahedral sites are occupied by cations. Each octahedron unit cell shares an edge with the following cell. These edge-sharing octahedral are considered to facilitate the electron transfer. As a result, rutile structured materials can exhibit high electronic conductivity (*42*). Oxygen vacancies can be introduced to rutile lattice; however, the mobility of oxygen vacancies on these structures is low, causing low ion conductivity, and thus reducing the performance of the fuel cell.

Perovskite structured materials have also been investigated as anode materials. Among these, chromite and Titanates oxides have been identified as promising anode electrodes (*56, 57*) . Lanthanum strontium Titanates of the form $(La_2Sr_4Ti_6O_{19-\delta})$ have been shown to exhibit high conductivity and low polarization resistance under extreme reducing conditions (*58*). Yttrium doped $SrTiO_3$ materials have also been proposed as anode materials (*59, 60*). However, achievement of high ionic conductivity requires reduction with gaseous H_2 at 1400 °C, resulting in degradation of other fuel cell components. Recent investigations have shown that $La_{0.6}Sr_{0.4}Co_{0.2}Fe_{0.8}O_3$ may be used as high performance anode electrodes, however stability of this material remains an issue (*61*).

2.5 Cathode electrode materials

The requirements for cathode electrodes are similar to those of anode electrodes, except that the environment characteristics of the cathode are oxidizing and the desired reaction is the oxygen reduction. Initial fuel cell designs used noble metals as the cathode electrode. However, their application is limited by its high cost (*5*). Alternatively, several perovskite oxides including lanthanum cobaltate and lanthanum manganite materials have been studied as cathode electrodes. Lanthanum manganite ($LaMnO_3$) perovskites attracted much interest for the development of YSZ-based fuel cells due to its electronic conductivity and its chemical stability. Research studies have demonstrated that introduction of cation deficiencies on the $LaMnO_3$ structure has the effect of inhibiting reactions at the electrode-electrolyte interface (*62, 63*). Particularly, strontium doped lanthanum manganite (LSM) has been found to prevent the formation of intermediate zirconium layers with YSZ electrolytes under operation conditions without affecting the oxygen ion transport. Further studies on LSM electrodes for YSZ-based fuel cells have shown that performance can be improved by using a multilayer structure composed of a thin dense LSM layer contacting the electrolyte over which, a second porous layer is applied (*64*).

Different doped lanthanum cobaltate perovskites have also been studied as cathode materials (*65-67*). Among these, $La_{1-x}Sr_xCoO_{3-\delta}$ (LSC) perovskites have attracted research interest due to its higher ionic conductivity when compared with LSM cathodes (*66*). Unfortunately, LSC has been shown to react with YSZ at the electrode-electrolyte interface, making it unsuitable for YSZ-based fuel cells. Alternatively, LSC performance is favored when Ceria electrolytes are used (*67*). Further studies on have reported the presence of a metal-insulator transition in LSC materials depending on the strontium content, temperature and oxygen partial pressure (PO_2) (*68*). Introduction of different dopants have been explored in order to improve LSC stability, including replacement of Lanthanum with Gd, and Sm. (*66, 69*). Recent studies have reported the successful implementation of $Sm_{1-x}Sr\ CoO_3$ cathodes on low temperature fuel cells based on Ceria electrolytes (*70*). Other related perovskite materials studied include Lanthanum Strontium Ferrites (LSF), Lanthanum, Lanthanum Strontium Cobaltite Ferrite (LSCF), Lanthanum Strontium Manganite Ferrite (LSMF), Samarium Strontium Cobaltite (SSC), and Lanthanum Calcium Cobaltite Ferrite (LCCF) (*71*).

2.6 SDC based IT-SOFCs.

Development of Intermediate temperature fuel cells based on SDC electrolytes require a systematic study on the different parameters affecting the fuel cell performance, including fabrication procedures, fuel cell architecture, type of electrodes employed, type of fuel used, and operation conditions. Although several studies on SDC based IT-SOFC have been reported, there is no general consensus on appropriate fabrication procedures, electrode materials, and operation conditions.

2.6.1 SDC electrolyte synthesis procedures

Fuel cell materials require special fabrication procedures in order to achieve the required chemical composition as well as the desired physical properties. Most fabrication procedures start with special chemical synthetic procedures that lead to materials having very specific distribution of their components. Electrolyte materials such as SDC has been prepared according to different advanced ceramic processing techniques including the hydrothermal synthesis method (*72*), the Oxalate co-precipitation method, the carbonate co precipitation, the glycine nitrate method and the pechini method. These techniques use different precursors and additives, and undergo a number of intermediate stages in order to obtain a final product with the exact composition, the highest purity and homogeneity. Among them, the pechini method stands out because of its simplicity, low cost, and high quality of the final ceramic powder.

2.6.1.1 The pechini process

In the pechini process, an aqueous solution containing the desired metal oxides or salts are mixed with an alpha hydroxycarboxylic acid such as citric acid inducing a chelation process. During chelation, formation of complex ring shaped compounds around the metal cations takes place in solution. Then, the solution is heated to 150 to 200 °C and polyhydroxy alcohol is added. The chelates undergo a polymerization forming large cross-linked networks. Excess water is removed by heating resulting in a solid polymeric resin. Further heating results in a decomposition of the resin yielding a mixed oxide material. The resulting material has very small particle size, typically between 20 and 50 nanometers, (although cluster agglomeration occurs) and homogeneous composition with intimate mixing.

2.7 SOFC Architectures

SOFC systems can be constructed according to different shapes depending on the stack design. Designs include tubular, flat plate or planar, bell and spigot, banded and corrugated structures. Among these possible designs, tubular and planar fuel cells have attracted majority of the research efforts. Figure 2.4 present a sketch of the tubular and the planar fuel cell designs.

Each design incorporates different cell configurations or architectures, which can be classified in to two general categories; self supported fuel cells and externally supported fuel cells. In the self supported fuel cells, one of the fuel cell components acts as the mechanical support; therefore there are anode supported, electrolyte supported and cathode supported fuel cells. Figure 2.5 present a schematic representation of the anode and cathode supported fuel cell architectures.

2.7.1 Electrolyte supported architectures

Electrolyte supported fuel cells have higher mechanical strength when compared to anode or cathode supported fuel cells due to the formation of a dense thick layer of electrolyte material. Anode and cathode materials require a porous structure to improve the accessibility of the gases to the reaction sites; therefore achievement of high density is usually limited. On the other hand, thick electrolyte layers result in large ohmic losses, leading to a reduction of the fuel cell performance.

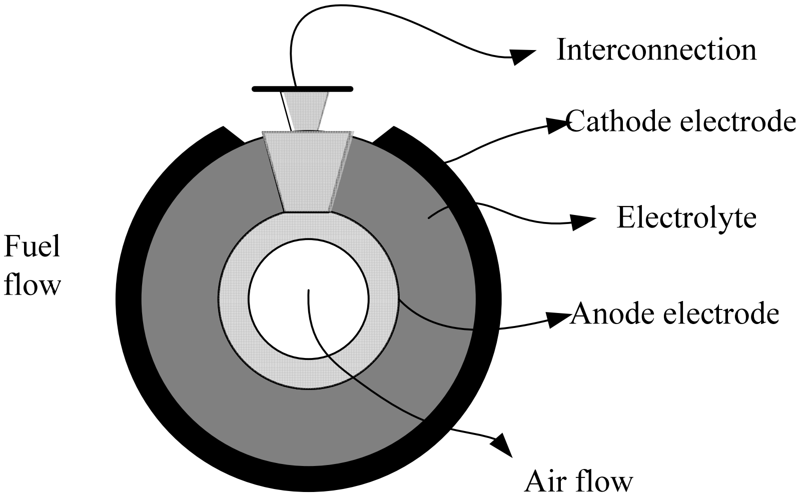

A. Tubular design

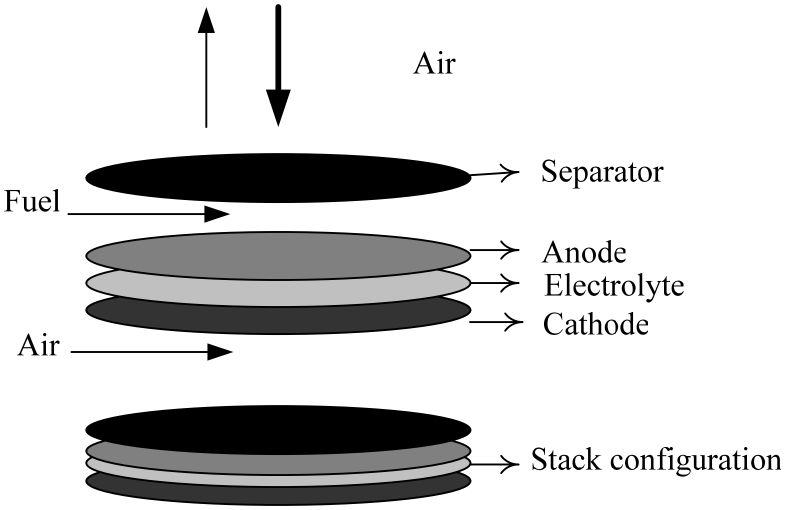

B. Planar design

Figure 2.4 Fuel cell designs: (A) Tubular design, (B) Planar design.

2.7.2 Anode supported architectures

The fabrication of anode supported fuel cells having acceptable mechanical strength requires processing of the starting powders at relatively high temperatures. In the case of Ni based anode cermets, sintering temperatures in excess of 1400 ºC allow the densification of the material without affecting the its electrochemical activity. However, the densification process leads to a reduction of the porosity of the electrode, causing transport limitations that affect the fuel cell performance.

2.7.3 Cathode supported fuel architectures

Cathode supported fuel cells have advantages for applications where the anode porosity is not a major concern. (i.e. the use of solid fuels such as coal) The majority of the fuel cell resistance is then concentrated on the cathode electrode. Most cathode materials require a relatively low calcinations temperature (~ 900 ºC) in order to generate the electrochemical activity, however, the connectivity between the electrolyte and the cathode electrode requires higher calcination temperatures. Additionally, higher temperatures have the effect of reducing the porosity of the material, reducing the available area for the oxygen reduction. Therefore, the cathode calcination temperature requires a careful balance between activation for the electrochemical activity and the microstructure and conductivity.

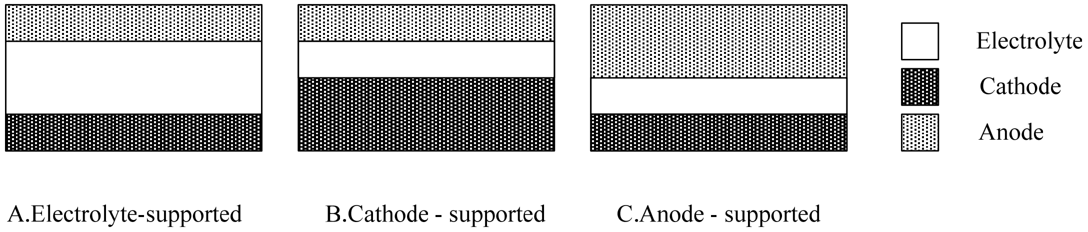

Figure 2.5 Fuel cell architectures: (A) Electrolyte supported, (B) Cathode supported, (C) Anode supported.

2.8 Processing of solid oxide fuel cell materials.

The processing of fuel cell materials is a very demanding and complex task due to the specificity of its components, the large number of variables affecting the proprieties exhibited by the materials, and its impact on the overall fuel cell performance. In order to meet the required specifications it is important to establish a stringent quality monitoring through all the fuel cell fabrication process.

Currently there is no guideline for the fabrication of fuel cells systems since the specific details on each fabrication steps vary depending on the selected working electrodes, the electrolyte material, the type of fuel employed, and the operating temperature, among others. Therefore, the development of a new fuel cell system requires at some point experimentation and trial and error. Regardless of this situation there are a few recommendations regarding some of the main aspects that must be controlled during the solid oxide fuel cell fabrication process, such as the selection and preconditioning of starting materials, the forming and drying step, and the sintering step. The following paragraphs discuss in a brief manner some of those aspects. For further descriptions there are many references that can be consulted.

2.8.1 Selection or starting fuel cell materials

The selection and pretreatment of starting materials is one of the most decisive factors affecting the performance of the fuel cell. Aspects such as chemical composition,

impurities, stoichiometry, phase, particle shape, and particle size distribution must be carefully considered.

2.8.1.1 Chemical Composition & Phase

The chemical composition of the starting materials employed on fuel cells should be fixed and constant. This condition is seldom met with powders containing transition metals because of their variable valency (i.e. the metal oxide can have a wide range of metal to oxygen ratios). Also, the presence of impurities can affect the dispersion of the powder in slurries, modify the sintering behavior, cause anisotropic grain growth, or alter specific final properties such as electron or thermal conductivity. Phase can also affect physical properties of raw materials such as specific surface area, density, and compatibility with other solid phases, even when the nominal chemical composition is the same. The specific phase of the material can affect the activity of the powder. Usually, in low temperature phases, the specific volume of the powder is larger compared to the high temperature phases, causing the sintering process to start at a lower temperature. With the right heating schedule the sintering process can be started at low temperature. However, phase transformation occurring during heating may cause damage on the sintered material due to reduction of the material specific volume. For these reasons, special care must be taken on the development of synthesis procedures yielding fuel cell grade materials.

2.8.1.2 Particle size & particle size distribution

Particle size and particle size distribution of starting powders have a strong impact over the material sintering rate and sintering temperature. Theoretical analysis have shown that sintering rate varies with respect to the particle size according to equation A

$$r\alpha\ p^{-3/4} \qquad (Eq\ 2.8)$$

Where "*r*" represents the densification rate, and "*p*" represents the particle size. Small particle introduces other difficulties such as the dispersion in slurries. The amount of dispersant needed is proportional to the surface area of the powder since the molecules of the dispersant must cover a considerable fraction of the particle surface area to generate the repelling interaction among particles. As a result, a very fine powder requires very large amounts of dispersant to disperse. If handled improperly, the small particles tend to form agglomerates that lead to fracture during sintering.

The particle size distribution directly affects the packing density of the material. Therefore a balanced proportion between coarse and fine particles must be met to achieve high density. Large particles create void space, reducing the maximum achievable density. Therefore introducing a particle size distribution helps improve the density of the material. Large particles also act as nuclei for grain growth creating abnormal sintered particles with detrimental effects on the material properties. On the other hand, broad particle size distributions promote exaggerated grain growth during sintering.

Particle shape has also an effect on the packing structure of the material. High packing densities are achieved with particles with a shape near to spherical shape. Particles having needle or platelet shape randomly oriented leave empty hence does not create high density. Also, shear stress tends to orientate needle or platelet particles forming unique microstructures of anisotropic properties. Therefore they become more difficult to process if extrusion or injections molding processes are to be used.

2.8.2 Grinding of fuel cell materials.

Reduction of particle size is one of the most common preconditioning steps in the processing of fuel cells materials. In general, there are two major approaches to produce fine powders, breakdown and build up process. In breakdown processes, particle size is reduced by means of mechanical action. (i.e. grinding) Most breakdown techniques are able to produce limit particle sizes as small as 1 mm. In contrast, build up processes such as chemical vapor deposition (CVD) are able to produce particle sizes as big as 0.1 mm. Recent advances on grinding technology have managed to achieve particle sizes between 1mm and 0.1 mm, overcoming what before was referred as the valley in the range of submicron particle powders. There are two major mechanisms to obtain fine particles, volume grinding and surface grinding. On volume mechanisms, solid particles are broken into smaller components by impactation. On surface grinding mechanisms, very fine particles are produced from the surface of the solid particles by frictional forces. Frictional mechanism is more effective for the production of submicron particles, and it is often applied on a variety of milling machines including roller milling, and ball milling. Additional details on the characteristics can be found on specialized publications.

2.8.3 Introduction of Processing Additives.

Interaction between particles such as Van der Waals forces, favor the formation of aggregates and big particles affecting the properties of the final product. Therefore most common processing techniques include a step for introducing processing additives. Most common additives include Binders, dispersants, lubricants, and plasticizers. The selection of additives and their relative concentration depends on the characteristics of the specific fuel cell material as well as on the selected forming process (i.e. dry pressing, injection molding etc). During typical processing procedures a solvent of a set of solvents are mixed with the fuel cell powder material and the different additives are incorporated. Dispersants are added in order to break apart particle agglomerates and ensure well dispersed slurries. Binders provide strength to the body of the fuel cell during the forming and sintering step. Lubricants and plasticizers are introduced to facilitate injection molding procedures.

CHAPTER III

EXPERIMENTAL

3.1 Synthesis of Samarium Doped Ceria (SDC) Electrolytes.

Cerium III nitrate 99.5%, samarium III nitrate 99.9%, ethylene glycol 99 + % and citric acid monohydrate ACS 99.0 % were purchased from Alfa Aesar and used without further purification to synthesize SDC electrolytes. More detailed specification of the reagents used is presented in table 3.1

Samarium doped ceria SDC electrolytes with a 20 % mol samarium dopant content ($Sm_{0.2}Ce_{0.8}O_{1.9}$) were prepared according to the pechini method. In this technique, nitrate compounds of the desired metals and a chelating agent are employed as the starting materials in order to obtain a well distributed homogeneous ceramic powder. During the process, stoichiometric amounts of each metal nitrate were weighted and dissolved in water at room temperature. The resulting material was mixed with a solution of citric acid and ethylene glycol (1.88 molar metal to citric acid ratio), and was allowed to undergo three consecutive steps: polymerization, solvent removal, and calcination. A typical synthesis procedure is as follows. 3.09 g of cerium nitrate and 0.79 g of samarium nitrate were weighted and dissolved in deionized water at room temperature.

In a separate beaker, 5.86 g of a solution containing citric acid and ethylene glycol (60 % wt citric acid) was prepared. The above two solutions were then mixed under vigorous stirring at 70 °C. The resulting mixture was further heated to 90 °C and was allowed to react for several hours until yielding yellowish foam like material.

The obtained foam was removed from the beaker, placed in an alumina crucible, and calcined at 450 °C for 5 h at a heating rate of 5 °C / min. Finally, the material was crushed using a hand and pestle mortar to obtain a fine cream colored powder. The resulting SDC powder was dried milled for 24 h using a rotary ball milling device using a plastic container with ceramic grinding balls. The obtained material was dried for 2 hr at 120 °C, passed through a #120 sieve (125 µm size), and then calcined at 900 °C for 6h at a heating rate of 5 °C /min.

3.2 Samarium Strontium Cobaltite (SSC) electrodes.

Samarium (III) oxide 99.9%, cobalt oxide (II, III) 99%, and strontium carbonate 99.99% were purchased from Alfa Aesar and were used without further purification to synthesize SSC electrodes. A summary of the specifications on the reagents used is presented in table 3.2.

Table 3.1 SDC reagents.

Reagent	**CAS Number**	**Formula**	**Formula weight**	**Form**
Samarium III nitrate	13759-83-6	$Sm(NO_3)_3*6H_2O$	444.45 (336.36 anhy)	Crystalline
Cerium III nitrate	10294-41-4	$Ce(NO_3)_3*6H_2O$	434.22 (326.13 anhy)	Cristalline Aggregates
Citric acid	5949-29-1	$C_6H_8O_7 \cdot H_2O$	210.14 (192.13 anhy)	Solid
Ethylene Glycol	107-21-1	$HOCH_2CH_2OH$	62.07	Liquid

Samarium Strontium Cobaltite electrodes with a molar composition corresponding to 0.5 mol of Samarium, 0.5 mol of Stronium and 1 mol of cobalt $Sm_{0.5}Sr_{0.5}CoO_3$) were prepared by mixing stoichiometric amounts of samarium oxide, cobalt oxide, and strontium carbonate and calcining the mixture at 800 °C.

A typical synthesis procedure is as follows. 2.32 g of samarium oxide, 3.20 g of cobalt oxide and 0.98 g of strontium carbonate were weighted and mixed in methanol. The resulting mixture was wet ball milled for 24 h using a plastic container and ceramic grinding balls. The obtained material was dried for 2 hr at 120 °C and then calcined at 800 °C for 6h at a heating rate of 5 °C /min.

3.3 Characterization of fuel cell materials

XRD diffraction patterns of samarium doped ceria ($Sm_{0.2}Ce_{0.8}O_{1.9}$) and strontium doped samarium cobaltite ($Sm_{0.5}Sr_{0.5}CoO_3$) powders were taken using a Philips PW1710 diffractometer with Cu-Kα radiation operated at 40 kV and 35mA and a scanning step of 0.020 degree. Raman spectra of the samarium doped ceria ($Sm_{0.2}Ce_{0.8}O_{1.9}$) and strontium doped samarium cobaltite ($Sm_{0.5}Sr_{0.5}CoO_3$) powders were taken using a Nicolet 560 Magna FT-Raman module spectrometer configured with a 2.0 W Nd:YEG laser operating at 1064 nm. Morphology of the prepared material was characterized using a scanning electron microscope (SEM) Hitachi S-2150. Discussion of the results obtained from these characterization techniques is shown in sections 4.1 and 4.2.

Table 3.2 SSC reagents.

Reagent	**CAS Number**	**Formula**	**Formula weight**	**Melting point**
Samarium III oxide	12060-58-1	Sm_2O_3	348.70	2300 °C
Strontium Carbonate	1633-05-2	$SrCo_3$	147.63	1100 °C
Cobalt (II, III) oxide	1308-06-1	Co_3O_4	240.80	900 °C

3.4 Ceramic processing of IT-SOFC materials

The fuel cell materials were further processed by adding a PVB (Poly Vinyl Butyral) based organic binder and a number of additives in order to enhance the strength of the ceramic material during the fuel cell fabrication process by creating what is referred to as green body. Different amounts of additives such as a binder, a dispersant, and a mixture of solvents were introduced during the preparation of the electrolyte and electrode green bodies, as summarized in table 3.3. During Green body preparation procedures 2.0 g of the fuel cell starting material (SDC or SSC) were weighted and added to a solution containing 1.5 g of isopropyl alcohol (Fisher chemical) and X mg of fish oil from menhaden (Sigma) at room temperature. The obtained slurry was subsequently grinded (wet milling) in a 3 lb laboratory ball mill containing zirconia balls for 7h. The resulting material was mixed with a solution of containing Y mg of a polyvinyl butyral-polyvinyl alcohol-polyvinyl acetate terpolymer organic binder BUTVAR®, 500 mg of isopropyl alcohol, and 500mg of 99.8% toluene (Alfa Aesar) and was grinded for three more hours. The resulting slurry was dried at room temperature for 2 h and finally re crushed using a hand and pestle mortar. Figure 3.1 presents a diagram illustrating the green body fabrication procedure.

3.5 Fuel cell Assembly

3.5.1 Disc preparation

Fuel cell discs were prepared using the dry pressing technique. 0.5g of SDC additive processed electrolyte powders (green body) were weighted, placed inside a stainless steel die and pressed at 250 MPa in order to shape them in the form of discs. The resulting discs were sintered in order to achieve densification of the electrolyte at 1500 °C for 5 h following a heating rate of 1 °C / min. During the initial step of the sintering, the binder and the rest of the additives are burned creating a capillary effect that attracts the particles together. After densification, the discs were further processed by applying a slurry of the electrodes fabricated using the described techniques. Pt current collectors were applied using a Pt ink (Engelhard HA3788A) and were fired at 950 C for 2 h in order to complete the fuel cell fabrication.

The fuel cell discs were then attached to alumina tubes and were sealed using a ceramic adhesive (Ceramabond 685-N Aremco Products Inc). The resulting fuel cell was placed inside an oven and was heated to the operating temperature at a heating rate of 1 ºC /min.

Table 3.3 Specific compositions for fuel cell material processing

Green Body material	**Weight (g) of Fuel cell material added**	**Weight (mg) of PBV Binder added (X)**	**Weight (mg) of fish oil added (Y)**
Electrolyte	SDC = 2	60	80
SDC-SSC	SSC = 1.4 SDC = 0.7	120	150

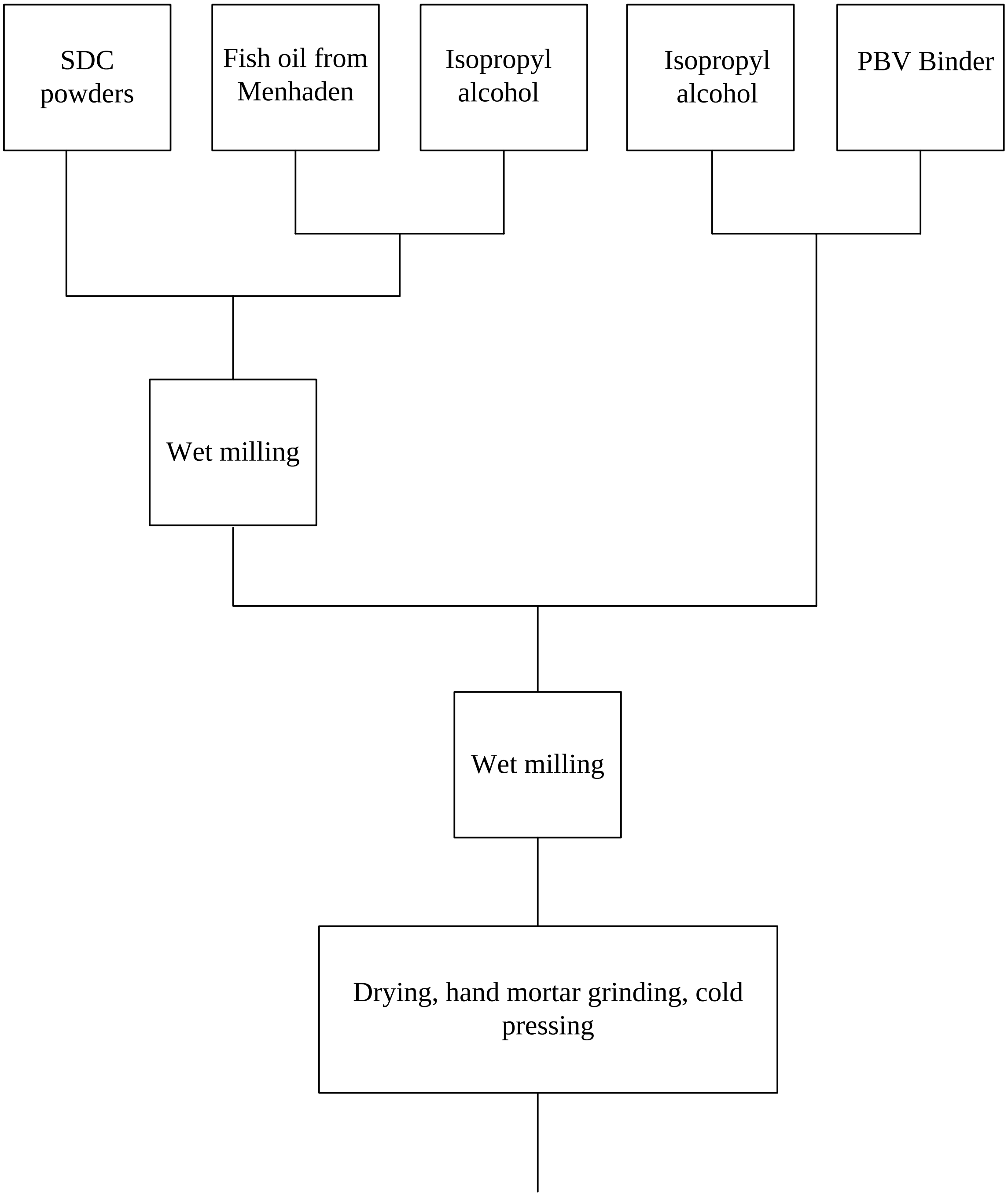

Figure 3.1 General procedures for the fabrication of ceramic materials

CHAPTER IV

FABRICATION OF AN ELECTROLYTE SUPPORTED FUEL CELL

Samarium Doped Ceria (SDC) and Strontium Samarium Cobaltite (SSC) were characterized and used with the purpose of fabricating IT-SOFCs operating between 600 and 800 °C. SDC electrolytes and SSC electrodes prepared according to the techniques described in the experimental section were characterized in order to determine their structure as well as their shape and particle size. Characterization techniques included X-Ray diffraction (XRD), Raman spectroscopy, and scanning electron microscopy (SEM).

Major fuel cell fabrication steps including the manufacture of electrolyte layers, the deposition of anode and cathode electrodes, the introduction of current collectors, and the sealing process were studied in order to establish a procedure that allows the manufacture electrolyte supported fuel cells. The following sections present a discussion on the results obtained from the characterization of fuel cell materials as well as from the adequate procedures for developing electrolyte supported fuel cells.

4.1 Characterization of Samarium Doped Ceria (SDC) electrolytes

SDC electrolyte materials having a 20% mol samarium dopant concentration ($Sm_{0.2}Ce_{0.8}O_{1.9}$) were characterized by X-Ray diffraction (XRD), Raman spectroscopy and scanning electron microscopy (SEM). Results are summarized in the following section.

4.1.1 X-Ray diffraction patterns

X-Ray diffraction patterns of the synthesized SDC electrolytes were taken using a Philips PW1710 diffractometer with Cu-Kα radiation operated at 40 kV, 35mA and a scanning step of 0.020 degree. Analyzed samples consisted of SDC powders calcined at 450 °C (first calcination step during fabrication procedure), 900 °C (second calcination step during fabrication procedure) and an SDC sample from a commercial source (Fuel cell materials) for comparison purposes. Results are in agreement with previous literature references (*1-5*), confirming the fluorite structure on all the samples. Peak broadening of the samples processed at low temperature were greater than those of the materials calcined at higher temperature suggesting that higher calcination temperature has an impact on crystallite size of the material. Similarly, peak broadening on the SDC powder samples synthesized following the procedures described in the experimental part was greater than that corresponding to the SDC samples obtained from the fuel cell materials, suggesting that the latter material posses larger crystallite size.

Lattice parameters (*1, 4-9*) and theoretical densities (*10, 11*) were measured and compared with experimental values reported in literature sources. Figure 4.1 presents XRD patterns for samples of SDC powders calcined at 450 °C, 900 °C and from Fuel cell materials. Table 4.1 presents lattice parameters and theoretical densities. Calculation of theoretical density of the synthesized electrolytes was performed using the lattice parameters by assuming the vacancy model. In the vacancy model, incorporation of dopants into the fluorite CeO_2 network generates vacancies according to equation 4.1, as mentioned in section 2.2.1.

$$\mathrm{xMO_{1.5} + (1-x)CeO_2 \rightarrow xM'_{Ce} + 0.5xV_{O}^{\cdot\cdot} + (1-x)Ce_{Ce}^{x} + (2-0.5x)O_{O}^{x}} \qquad \text{(Eq 4.1)}$$

Considering perfect face centered (fcc) fluorite structure having four atoms per unit cell theoretical density can be expressed as:

$$D_{vac} = \frac{4xM_d + 4(1-x)M_{Ce} + 4(2-\frac{x}{2})M_O}{N_A[a]^3}$$

where:
D_{vac} = density from vacancy model
M_d = Atomic weight of dopant cation
M_{Ce} = Atomic weight of cerium
M_O = Atomic weight of oxygen
N_A = Avogadro number

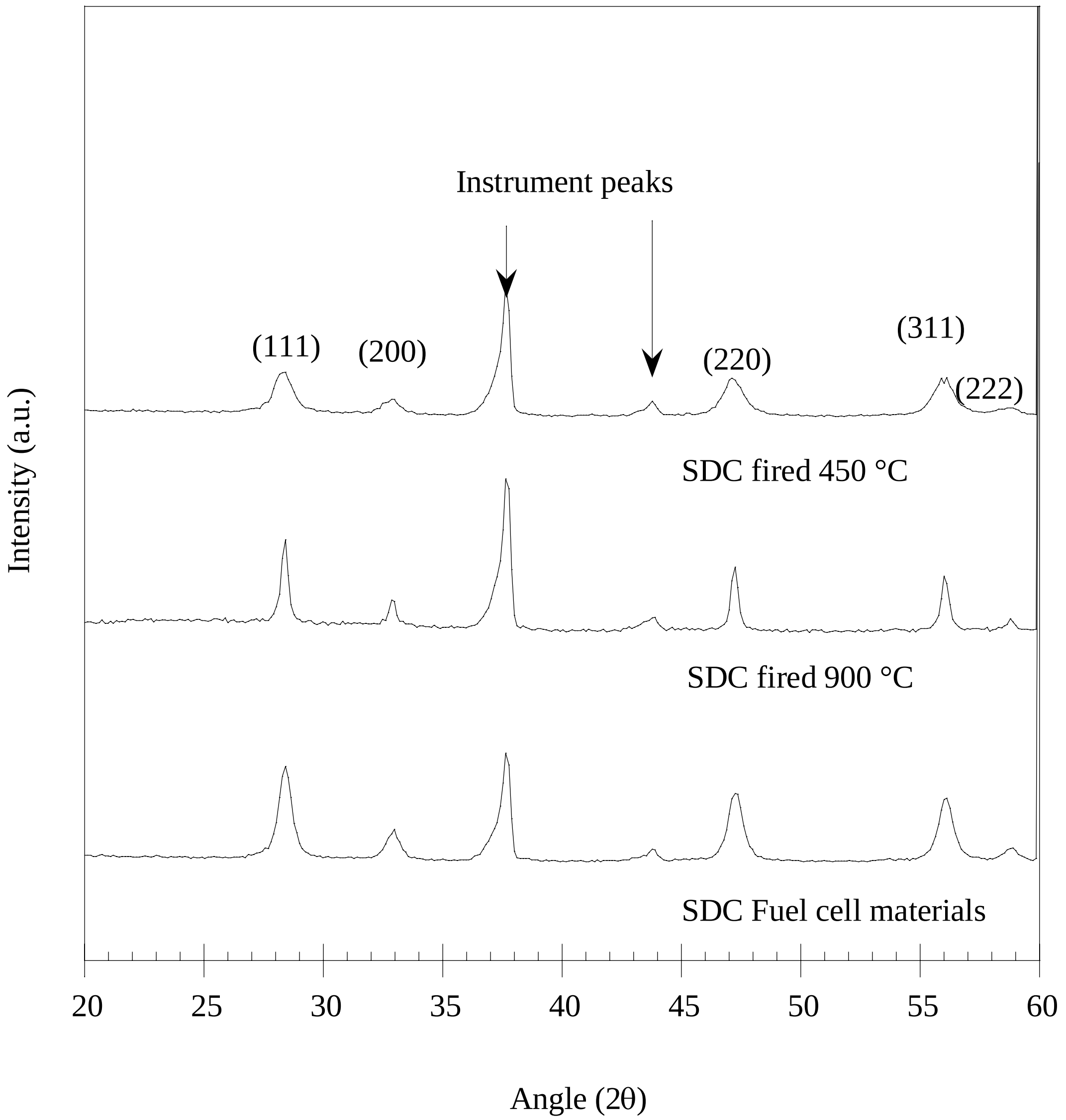

Figure 4.1: XRD patterns for SDC powders calcined at 450 °C, 900 °C, and from a commercial source (Fuel cell materials).

Table 4.1 Lattice parameters and theoretical densities for SDC

Sample (fabrication technique)	**Calcination Temperature (°C)**	**Lattice Constant (Å)**	**Theoretical density (g/cm^3)**	**Reference**
$Sm_{0.2}Ce_{0.8}O_{1.9}$ (Pechini Process)	450	5.437	7.129	This work
$Sm_{0.2}Ce_{0.8}O_{1.9}$ (Pechini Process)	900	5.426	7.172	This work
$Sm_{0.2}Ce_{0.8}O_{1.9}$ (Fuel cell materials)	-------	5.415	7.218	This work
$Sm_{0.2}Ce_{0.8}O_{1.9}$ (Carbonate precipitation)	700	5.438	7.125	(*10*)
$Sm_{0.2}Ce_{0.8}O_{1.9}$ (Oxalate precipitation)	600	-----	7.135	(*11*)
$Sm_{0.2}Ce_{0.8}O_{1.9}$ (Sol-gel method)	600	5.44	-----	(*9*)
$Sm_{0.2}Ce_{0.8}O_{1.9}$ (Hydrothermal process)	220	5.433	-----	(*5*)
$Sm_{0.2}Ce_{0.8}O_{1.9}$ (Microwave Combustion)	>1000	5.4299	-----	(*4*)
$Sm_{0.2}Ce_{0.8}O_{1.9}$ (Pechini Process)	700	5.437	-----	(*6*)
$Sm_{0.2}Ce_{0.8}O_{1.9}$ (mechano-chemical rxn)		5.435	-----	(*7*)
$Sm_{0.2}Ce_{0.8}O_{1.9}$ (Citrate method)	700	5.437	-----	(*8*)
$Sm_{0.2}Ce_{0.8}O_{1.9}$ (Solid state reaction)	1450	5.435	-----	(*1*)

4.1.2 Raman Spectra

Raman spectra of the SDC powders were taken using a Nicolet 560 Magna FT-Raman module spectrometer configured with a 2.0 W Nd:YEG laser operating at 1064nm. Analyzed samples consisted of SDC powders calcined at 900 °C and an SDC sample from a commercial source (Fuel cell materials). Results are in agreement with previous literature sources (*12, 13*), evidencing the only allowed band (F_{2g}) characteristic of fluorite metal dioxides (~ 460 cm^{-1}). In addition to the F_{2g} band, literature sources cite the presence of a broad band located in the range 540 – 600 cm^{-1} which has been assigned to the oxygen vacancies in the CeO_2 lattice (*14*). Raman results did not show evidence of this broad band, possibly due to lack of heat treatment. Figure 4.2 presents Raman spectra for synthesized SDC powders.

4.1.3 Scanning electron microscopy (SEM) images.

SEM micrographs of the SDC powders calcined at 900 °C were taken using a scanning electron microscope (SEM) Hitachi S-2150. Particle size was roughly estimated using the obtained SEM micrographs with the aid of image processing software (Sion image for windows). Results suggest an average particle size in the range of 5 to 20 µm. Figure 4.3 present SEM micrographs for the characterized SDC powders.

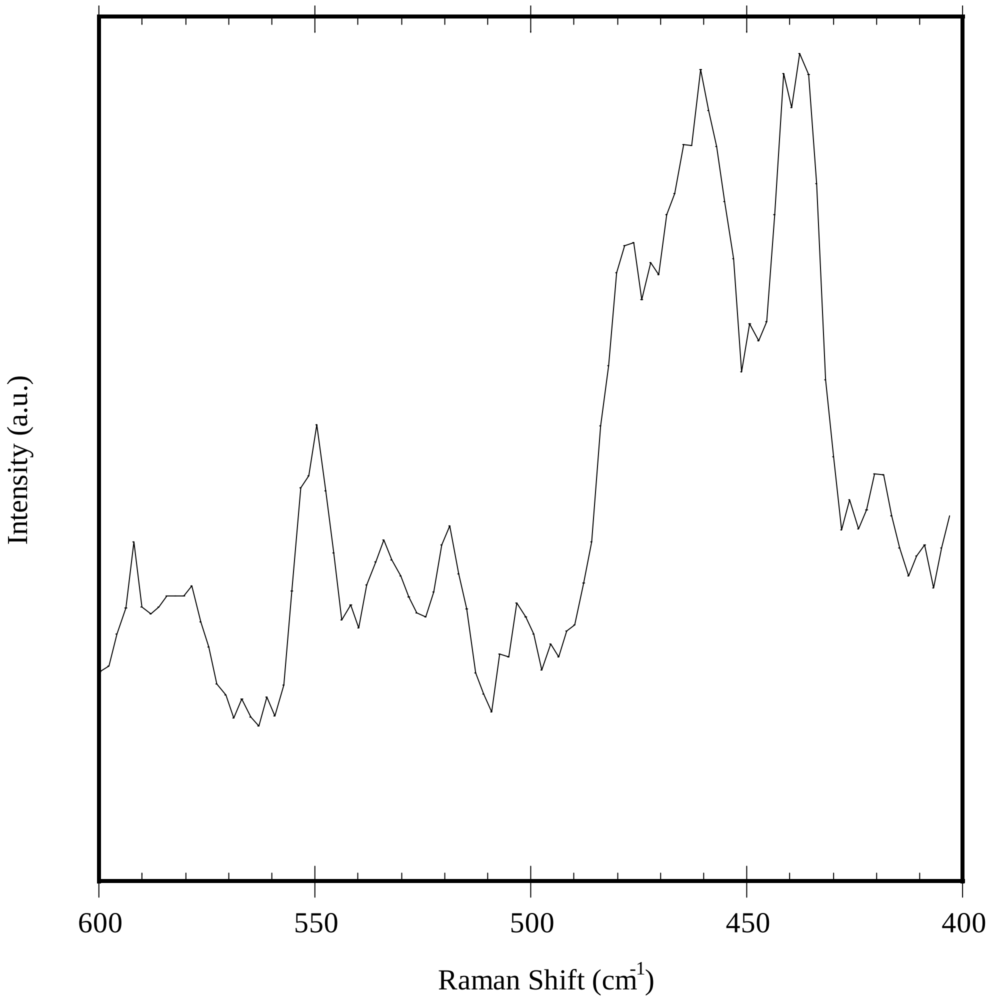

Figure 4.2 Raman spectra from SDC electrolyte material evidencing the band characteristic of fluorite metal dioxides at 460 cm^{-1}.

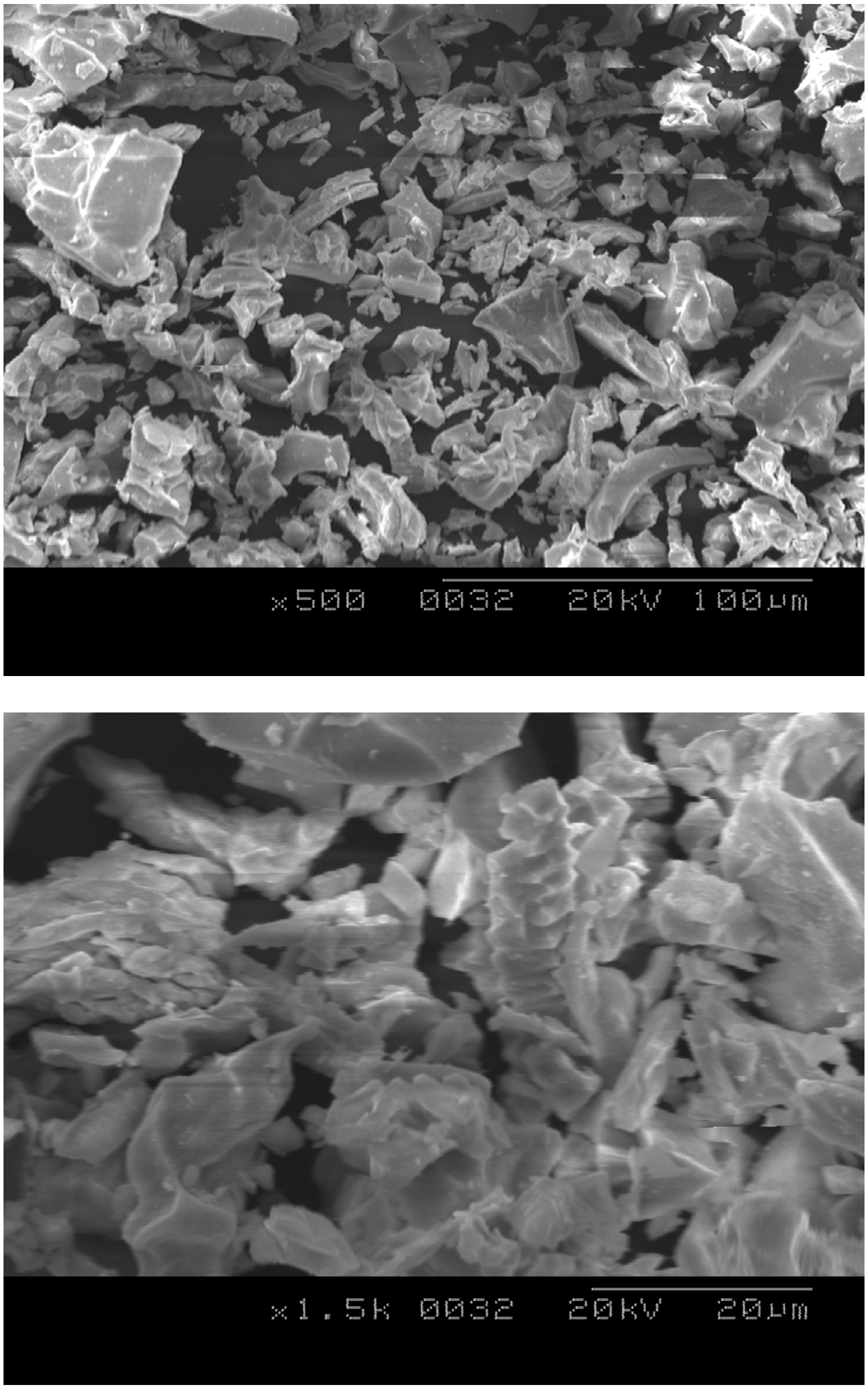

Figure 4.3 SEM micrographs of SDC powders calcined at 900 °C.

4.2 Characterization of SSC electrodes.

SSCC electrode materials with a 20% mol samarium dopant concentration ($Sm_{0.5}Sr_{0.5}CoO_3$) were characterized by X-Ray diffraction (XRD), and scanning electron microscopy (SEM). Results are summarized in the following section.

4.2.1 X-Ray diffraction

X-Ray diffraction patterns of the $Sm_{0.5}Sr_{0.5}CoO_3$ powders prepared and characterized as reported in the experimental section were consistent with previous reported XRD data on SSC electrodes (*15*), confirming the perovskite structure. Low intensity peaks such as that located at $2\theta = 42.5$ can be explained as residual diffraction peaks from starting materials (Samarium oxide, strontium carbonate and Cobalt oxide). Figure 4.4 presents XRD patterns for samples of SDC powders.

4.2.2 Scanning electron microscopy (SEM) images.

SEM micrographs of the SSC powders were taken using a scanning electron microscope (SEM) Hitachi S-2150. Particle size was roughly estimated using the obtained SEM micrographs with the aid of image processing software (Sion image for windows). Results suggest an average particle size in the range of 4 to 7 µm. Figure 4.5 present SEM micrographs for this material.

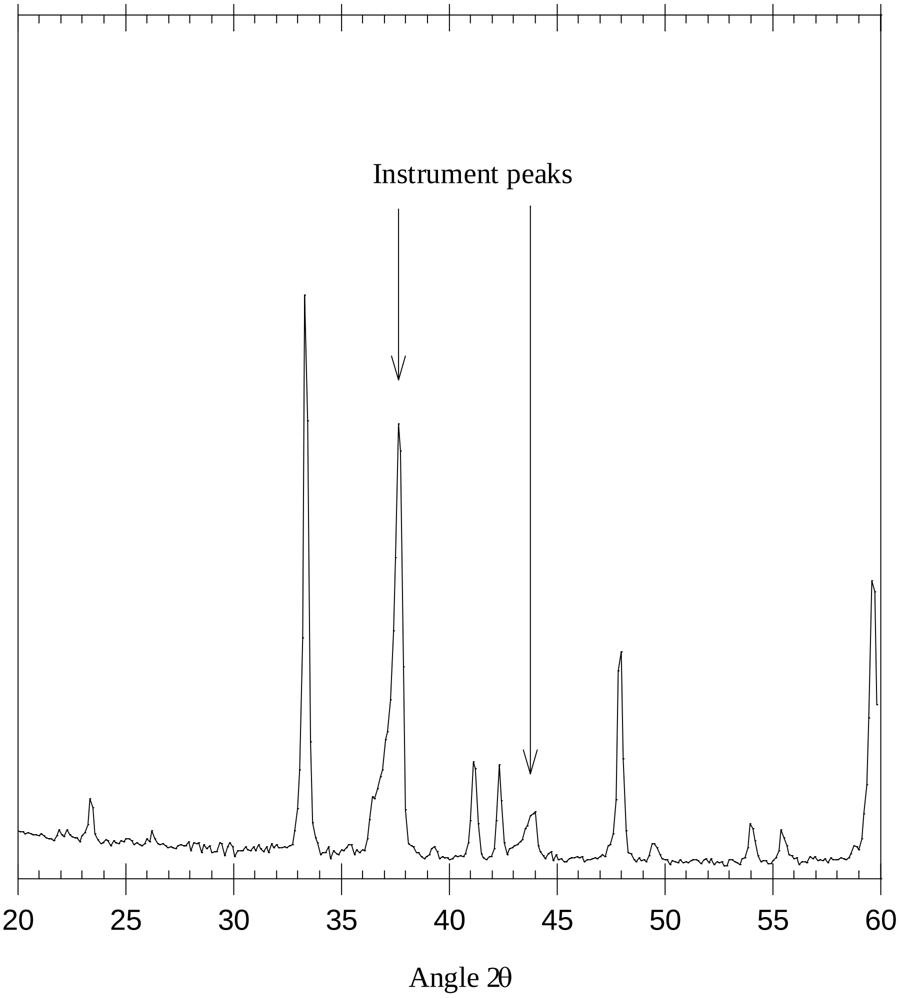

Figure 4.4 XRD patterns of SSC electrode powders. Comparison with reported XRD patterns from SSC materials confirmed the perovskite structure.

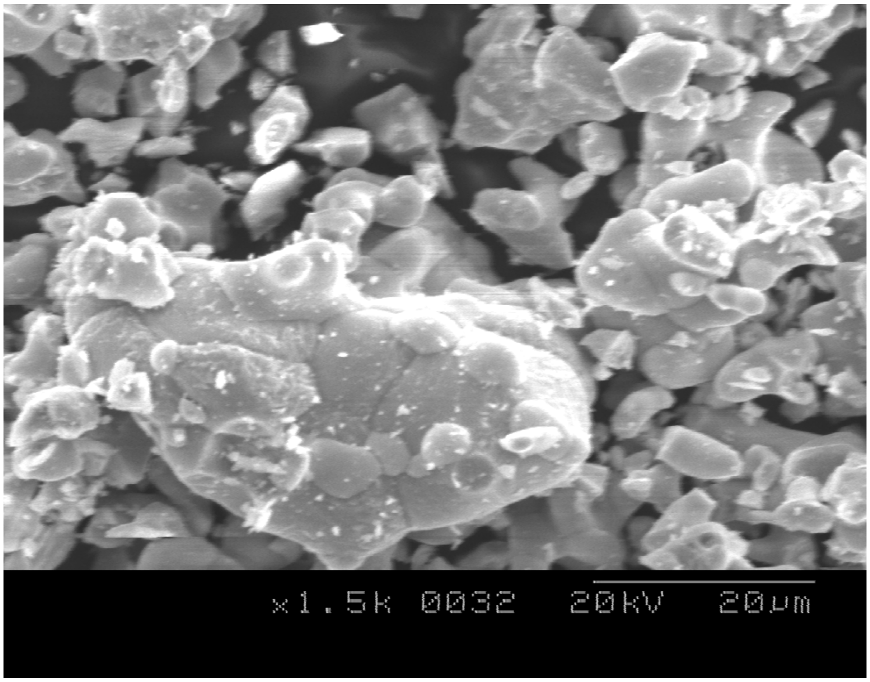

Figure 4.5 SEM micrographs of SSC powders

4.3 Preparation of solid electrolyte layers.

Fabrication of electrolyte supported SOFCs requires developing electrolyte layers that separate the anode from the cathode compartment preventing fuel, oxygen or electron crossover, while allowing oxygen ion diffusion and providing a robust support for the fuel cell assembly. Consequently, desired properties for electrolyte membranes include high electronic and ionic conductivity, high density, and mechanical strength. The following selections present a discussion on the selected experimental fabrication procedures used in this study and their impact on the properties of the electrolyte layers.

4.3.1 Selection of electrolyte Powders

As mentioned during the background section, the conductivity of Ceria-based electrolytes depends on type dopant, relative dopant concentration, and electrolyte synthesis procedure. Therefore, fabrication of electrolyte layers having appropriate conductivities (large ionic conductivity and small electronic conductivity) requires selecting the correct starting electrolyte powders. In order to ensure good electrolyte conductivity, 20% mol dopant SDC powders obtained Fuel Cell Materials were selected for the manufacture of electrolyte membranes over the SDC material made at our laboratory because of two major reasons: i) their larger crystallite and ii) their smaller property variability from batch to batch.

4.3.2 Densification of electrolyte powders

Fully densified (non porous) electrolyte membranes reduce the possibility of O_2 crossover from the cathode side into the anode compartment of the fuel cell, generating combustion reactions. Similarly, when operating with gaseous fuels, porous electrolyte layers facilitate fuel crossover to the oxygen side reducing the generation of electricity. For this reason, the selection of fabrication procedures for electrolyte layers must ensure the achievement of highly densified layers.

Conventional ceramic fabrication procedures consist of two major steps; a consolidation step and a sintering step. During the consolidation step, the ceramic powders are preconditioned by introducing a number of additives such as binders, lubricants and dispersants in order to modify their properties, then, the resulting materials are shaped into their final form. During the sintering step, the consolidated ceramics are heated according to specific temperature programs.

4.3.2.1 Consolidation of electrolyte powders

Different consolidation techniques such as cold pressing and tape casting have been used during the manufacture of SDC electrolyte layers, as it has been reported in literature sources (*16, 17*) . Among these, cold pressing was selected due to its versatility and relative simplicity.

Results obtained from this study concluded that a preconditioning step in which the SDC powders are ball milled in a solution containing a 4 wt % fish oil from menhaden and a 3 % wt polyvinyl butyral-polyvinyl alcohol-polyvinyl acetate ter-polymer (PVB) organic binder dissolved in a mixture of isopropyl alcohol and toluene results in a powder material that reduces the development of cracks during the pressing stage and facilitates the densification of the electrolyte layers.

Incorporation of fish oil from menhaden has been shown to facilitate breaking of soft electrolyte powder aggregates held together by weak interactions such as Van der Waals forces during wet ball milling of ceramic materials (*18*). Experiments conducted in this study established that the use of fish oil in concentrations close to 4 wt % (with respect to dry SDC powders) resulted in powders having improved resistance to cracking during cold pressing and subsequent sintering. Higher fish oil concentrations lead to formation of oil-like slurries difficult to compact by the cold pressing technique.

Small amounts of PVB have also been used during the processing of fuel cell materials (*19*) with the purpose of improving the strength of the compressed material and reducing the chances of developing cracks prior to the sintering step. PVB binders act by surrounding the surface of the ceramic powder particles generating a connected network when introduced in adequate solubilized quantities during the preconditioning step. Subsequent removal of solvents results on materials with higher bulk density and improved molding properties. The amount of binder required to achieve this effect is proportional to the specific surface area of the electrolyte powder. High surface area electrolyte particles require large amounts of binders in order to connect the particles together, leading to inconvenient situations where large amounts of solvents are required. Results obtained from this study determined that the use of a 3 % wt PVB on SDC powders having 40.2 m^2/g BET surface area results in a processed material having improved properties facilitating the molding and sintering of electrolyte layers.

After the preconditioning process, the electrolyte powders were introduced in a metallic die and were pressed at pressures in the range of 200-300 MPa. The use of pressures below 200 MPa resulted in compacted discs exhibiting fractures detectable before and after sintering (no healing process during sintering was observed). The use of higher pressures did not seem to cause any additional improvement on the electrolyte layers based on visual inspections. However, higher compaction pressure had a negative impact on the life cycle of the metallic die.

4.3.2.2 Sintering of electrolyte layers

Sintering of compacted electrolyte layers in order to obtain high density layers requires establishing adequate sintering temperature and heating rate. Previous studies on Ceria-based electrolytes produced by the solid-state reaction method have reported sintering temperatures in the range of 1400-1700 °C (*20-25*). Recent research studies have lead to the development of wet-chemical techniques that allow densification at lower temperatures (*25-28*).

In order to establish suitable conditions for the densification of SDC electrolyte layers a number of discs were fabricated and sintered at three different sintering temperatures (1400, 1500, and 1600 °C) following heating rate of 1°C/min. Densified discs were visually inspected in order to detect the presence of fractures and defects. Densification of the discs was estimated by monitoring the disc diameter shrinkage during sintering, and by XRD density estimation.

Results obtained from this experiment determined that a sintering temperature of 1500 °C and a heating rate of 1 C°/ min allowed fabricating SDC electrolyte layers highly densified and free from fractures. The use of a higher sintering temperature (1600 °C) caused adhesion of the electrolyte layer to the adjacent Zirconia plates used during the heating process. This adhesion problem may be related to larger ceria diffusivity, as it has been mentioned by Jung (*20*) in a previous study. The use of a sintering temperature of 1400 °C produced discs with lower density (when compared to 1500 °C) with no major defects. Table 4.2 presents a summary of the experimental results.

Sintering theories (*29*) have described the densification of ceramic powders considering the starting material as a collection of packed agglomerates and a number of pores (void spaces) defined by the surface of adjacent agglomerates. Simplified representations of such pores consider them as polyhedron figures having specific volume; shape, dihedral angle and coordination number (number of touching particles bounding the pore surface). Figure 4.6 presents a schematic representation of the packed agglomerates and the pores dihedral angle and coordination number.

For a given dihedral angle, pores of high coordination number possess convex surfaces whereas pores of low coordination number posses concave surfaces. The change between concave and convex surfaces is characterized by a critical coordination number

(Rc). Direct observations have shown that if particles are not disrupted during heating, touching particles develop bridging necks by either evaporation-condensation or diffusion related processes. After neck formation further mass rearrangements occur in order to produce a pore surface morphology determined by the pore coordination number. Thermodynamic considerations lead to the conclusion that only pores having coordination numbers smaller than the critical coordination number (R<Rc) are able to disappear during sintering (*30*). As a result, achievement of highly dense electrolyte layers after sintering step requires eliminating pores of high coordination number.

In order to overcome the effect of high coordination pores during the sintering step and achieving higher densification on the electrolyte layers a hypothesis was formulated and tested. According to this hypothesis, reduction of pore coordination number can be achieved by increasing the powder particle size distribution.

The line of reasoning behind this hypothesis, which was inspired on previous research efforts on packing of spherical particles (*31*), can be easily depicted by considering the hypothetical sintering process of powders consisting of spherical particles of equal size, as presented in figure 4.7. Sintering of this powder requires diffusion of large amounts of material in order to fill the pores between the spherical particles. Introduction of particles with a broad size distribution allows filling the void spaces between the particles in a more effective way and therefore produces a highly packed product.

Table 4.2 Sintering behavior of SDC electrolyte layers.

Sintering Temperature (°C)	**% Diameter shrinkage**	**Density (g/cm^3)***
1400	19.14	7.1251
1500	21.80	7.1433
1600	--	--

* Density estimated from XRD patterns.

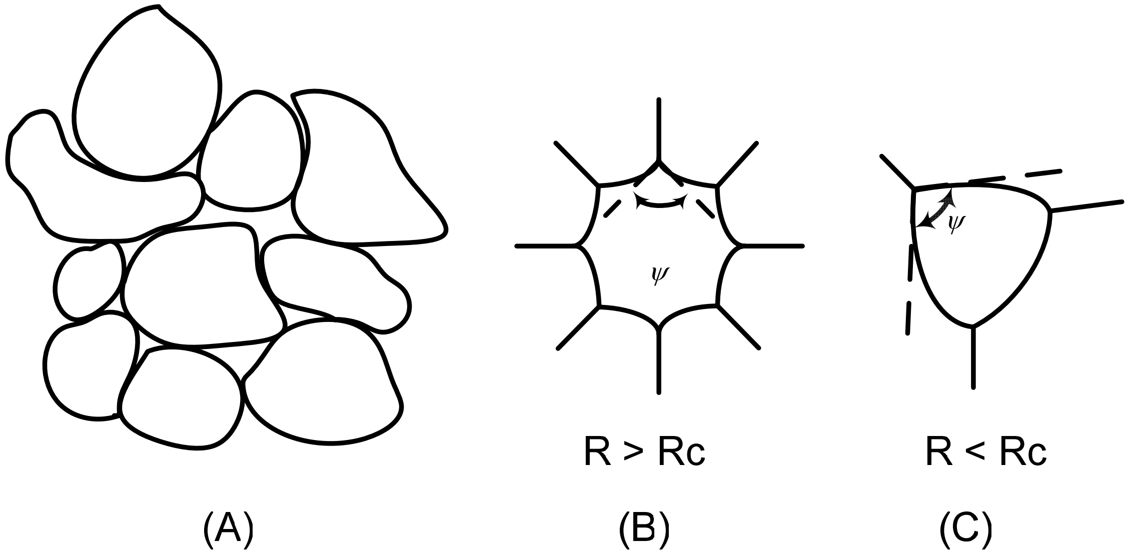

Figure 4.6 Schematic representation of (A) Packed agglomerates and pores in powder samples (B) Dihedral angle and pores of high coordination number and (C) Pores of low coordination number.

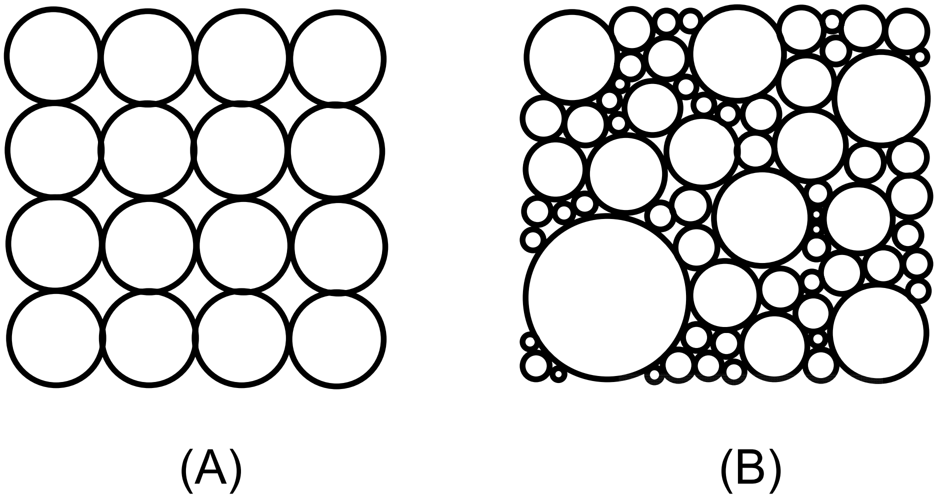

Figure 4.7. Schematic representation of (A) Equal size spherical particles and (B) Broad size distribution of spherical particles.

The approach proposed for broadening the particle size distribution consisted on mixing partially sintered powders with non pre-sintered powders. In addition to the elimination of highly coordinated pores, introduction of pre-sintered powders could benefit the densification of electrolyte layers because of the reduction of particle surface area, which has been shown to affect the rate of powder sintering (*10*). SDC powders were pre-sintered at three different temperatures in order to investigate the effect of a broader particle size distribution on the densification of electrolyte layers. The resulting materials were analyzed using a scanning electron microscope (SEM) Hitachi S-2150 in order to estimate average particle size. Figure 4.8 present SEM images for SDC powders pre-sintered at 1000, 1100 and 1200 °C.

Preliminary tests on the compression of pre-sintered SDC powders showed that the use of mixtures of 33 % wt pre-sintered and 66% wt non pre-sintered (fresh) powders resulted in discs having improved properties when compared to the corresponding mixtures of pre-sintered powders at 1100 and 1200 °C. This experimental observation could be related to the development of hard aggregates on pre-sintered powders at 1100 and 1200 °C.

SDC powders pre-sintered at 1000 °C mixed with SDC fresh powders were co-sintered at 1500 °C using a heating rate of 1 C °/ min. Results obtained from this experiment evidenced that the mixtures of pre sintered and fresh SDC powders are subject to smaller shrinking during densification. SDC electrolyte layers fabricated both, using only fresh SDC powders and using pre-sintered / fresh powder mixtures were further processed in order to test their performance during operation conditions.

A complete discussion on experimental results from these experiments is presented in sections 5.1 and 5.2.

4.4 Preparation of SSC electrode layers.

Fabrication of anode and cathode electrodes for electrolyte supported SOFCs requires developing a procedure for attaching the electrode material to the electrolyte substrate in such a way that the resulting electrode layer possess good contact with the electrolyte (increasing the three phase boundary), sufficient electronic conductivity, and large porosity. Common approaches for attaching electrodes to the electrolyte include preparation of co-pressed layers (*32*), and casting of slurries (*33*). Fabrication of SSC by the co pressing approach requires firing the multilayer structure at high temperature (~1500 °C) to achieve the SDC electrolyte densification. Preliminary experiments determined that SSC becomes unstable at temperatures in excess of 1200 °C. For this reason, the slurry approach was selected over the co-pressing approach.

Preliminary experiments on SSC slurries on SDC electrolyte layers determined that achievement of sufficient electronic conductivity on the SSC electrodes required incorporation of multiple slurry layers. Although introducing several SSC layers increases the electrode electronic conductivity (facilitating the electron transport on the electrode material) thicker SSC layers increase the fuel cell resistance for ion diffusion. As a result, development of high performance electrodes is a compromise between electronic conductivity and electrode thickness.

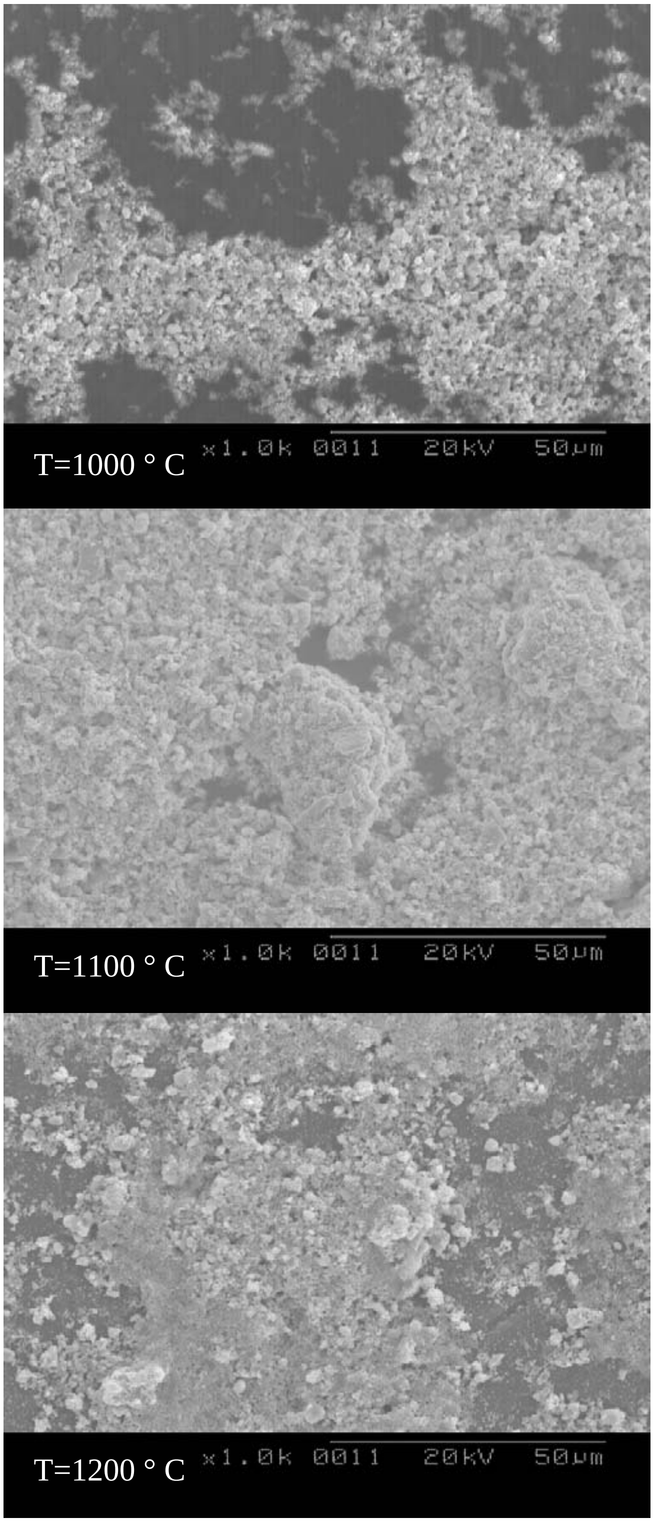

Figure 4.8 SEM images from SDC powders pre sintered at 1000, 1100 and 1200 °C.

SSC powders synthesized and characterized as mentioned in previous sections were used in order to develop anode and cathode electrode layers. SSC slurries were fabricated using appropriate amounts of binder, dispersant and solvents. The resulting slurries were smeared on both sides of the SDC electrolyte layers forming working electrodes of 0.5 cm^2 using a fine brush. Additional details on the fabrication of SSC slurries are described in section 3.4.

Preliminary experiments were carried out in order to estimate appropriate conditions (number of SSC layers) required for developing functioning electrodes with sufficient electronic conductivity and acceptable electrode overall thickness. During those experiments, multiple layers of SSC slurries were smeared, dried, and fired on the surface of an electrolyte layer and resistivity of the electrode layer was estimated at different positions after applying each electrode layer using a multimeter. Electrode thickness was estimated from SEM micrographs. Results from this experiment determined that application of two SSC slurry layers resulted in electrodes (after firing) having sufficient electronic conductivity and an average electrode thickness of 50 μm. Resistivity of SSC layers at different positions are presented in figure 4.9. SEM micrographs from SSC electrode thickness are presented in figure 4. 10.

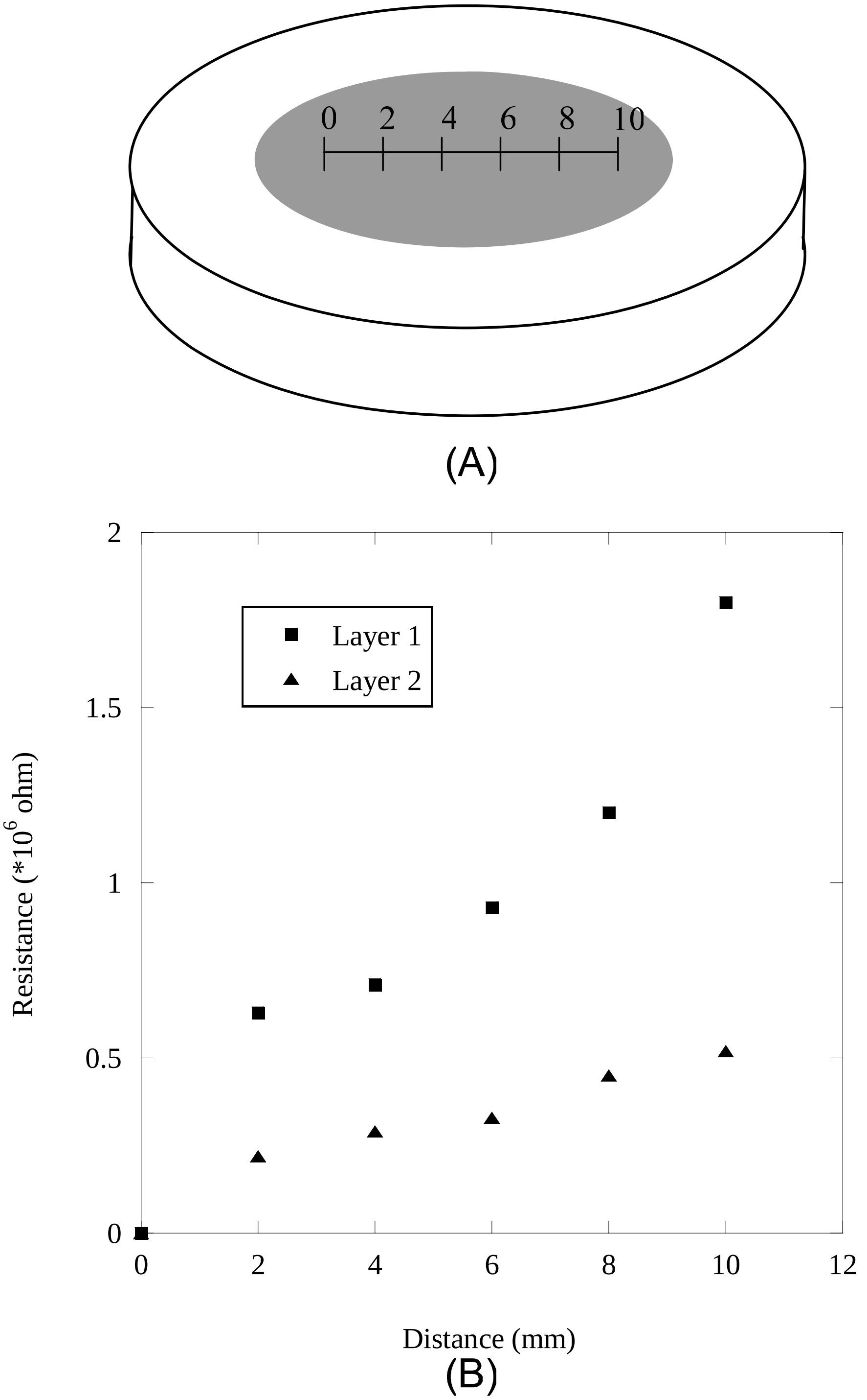

Figure 4.9 Electrode resistance measured at different distances from a reference point for each SSC layer applied (A) Sketch of positions measured and (B) Resistance measured.

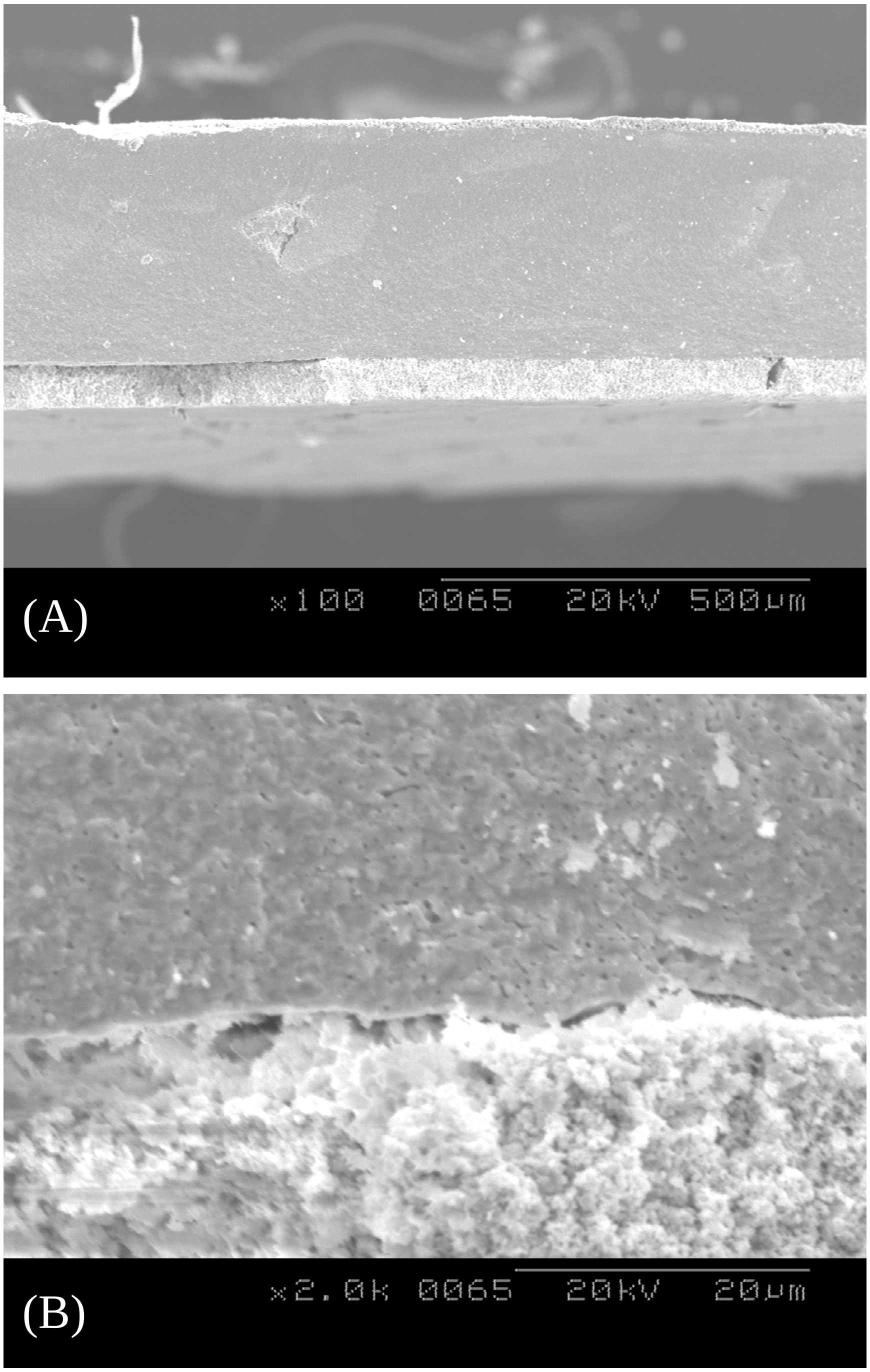

Figure 4.10 Electrode thickness after firing the second SSC slurry layer (A) Overall thickness (B) Magnification on electrode-electrolyte interface.

CHAPTER V

FUEL CELL PERFORMANCE

Electrolyte supported solid oxide fuel cells composed of an SDC electrolyte layer and two SSC layers acting as anode and cathode electrode were fabricated according to the procedures described in the experimental section in order to evaluate their performance. Different operating temperatures as well as fuel concentrations were tested by exposing the anode side of the fuel cell to various flow rates of gaseous H_2 while supplying O_2 from the air to the cathode side. Additionally, fuel cells made using SDC electrolytes processed with powders as received from the supplier and fuel cells fabricated with SDC powders heat treated (pre sintering fabrication approach) were tested in order to compare the effect of fabrication procedure in the fuel cell performance. Results from these experiments are presented in the following sections.

5.1 Effect of temperature on SOFCs performance

Electrolyte supported fuel cells fabricated using SDC powders obtained from a commercial source (Fuel cell materials) according to the procedures described in section 3.5 were tested at three different temperatures (600, 700, and 800°C) by flowing a mixture of 12.5 cc/min of He and 12.5 cc/ min of H_2 saturated at room temperature with H_2O (3% volume H_2O). *V-I* curves were recorded using a Labview ^{TM} software. Resulting *V-I* curves are presented in figure 5.1

Inspection of figure 5.1 allowed estimation of maximum power densities as well as open circuit voltages (OCV) at 600, 700 and 800 °C. Experimental OCV voltages are presented in Table 5.1. Previous research studies on SDC electrolytes have reported a decrease of the fuel cell OCV at higher temperatures under practical operation conditions (*1, 2*). This OCV reduction at higher temperatures can be explained by considering the development of electron conductivity on SDC electrolytes (causing electron crossing across the fuel cell) due to Ce^{+4} reduction at the anode side, as it has been discussed on different literature references (*3*).

Different approaches have been suggested in prevent the development of electronic conductivity on the anode side of SDC based fuel cells, including the coating of protecting layers, the use of alternative SDC synthesis procedures and the fabrication of YSZ-SDC solid solutions (*4-6*).

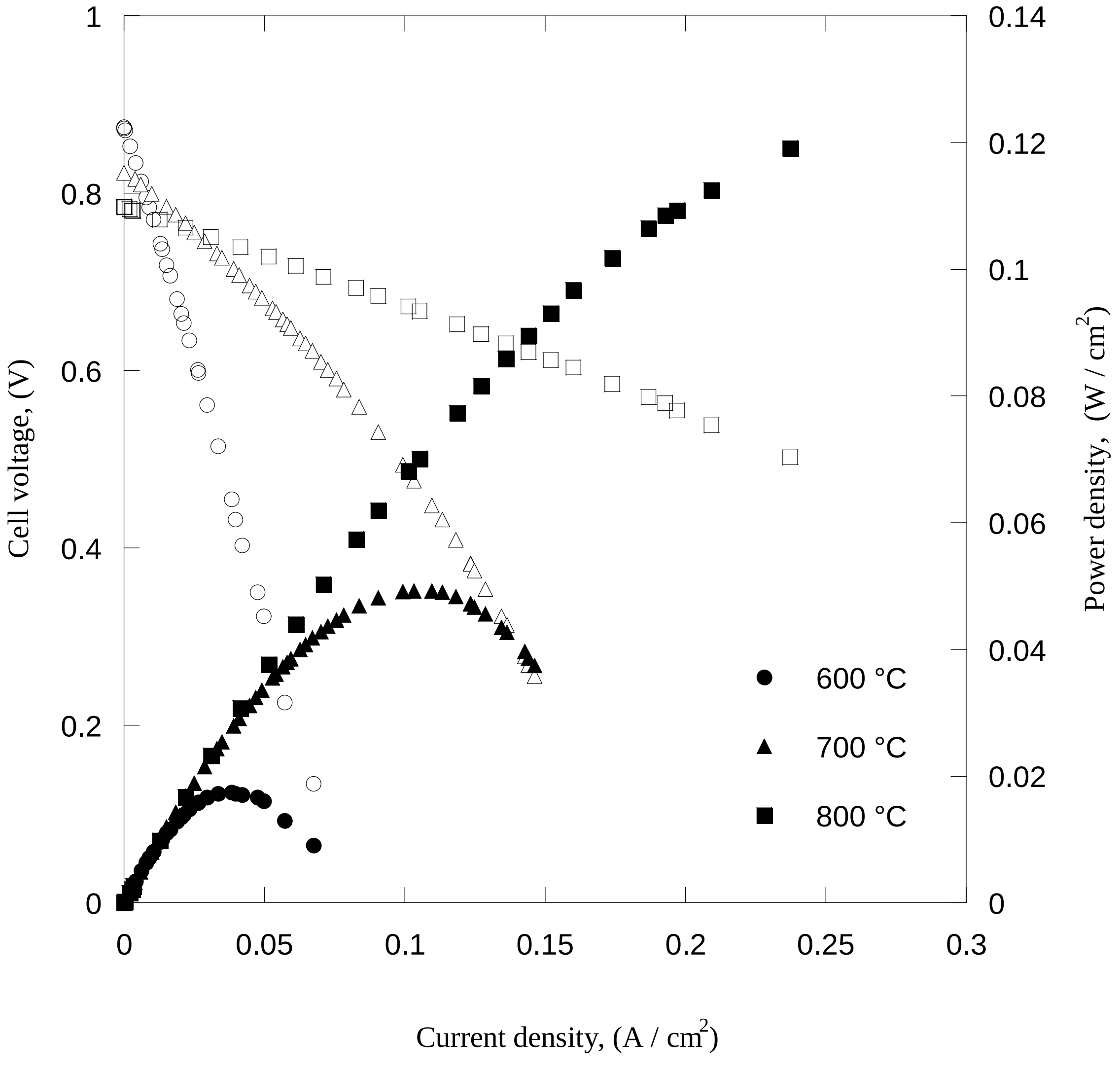

Figure 5.1 *V-I* curves (open symbols) and their corresponding power densities at 600, 700, and 800 °C for an electrolyte supported cell fabricated with SDC powders.

Table 5.1 Open circuit voltage (OCV) and Maximum power density for fuel cells fabricated using SDC powders without pre heating treatment.

Operating temperature (°C)	**OCV (Volt)**	**Max Power density (W/cm2)**
600	0.875	0.0178
700	0.816	0.0493
800	0.783	>0.12

5.2 Effect of fabrication procedure on SOFC performance.

Fuel cells fabricated using SDC a mixture of pre-sintered SDC and fresh SDC powders as mentioned in section 4.3.2.2 were tested at 700 and 800 °C by flowing a mixture of 12.5 cc/min of He and 12.5 cc/ ° min of H_2 saturated at room temperature with H_2O (3% volume H_2O). *V-I* curves were recorded using a Labview ^{TM} software. Results are presented in figure 5.2

Inspection of figure 5.2 allowed estimation of maximum power densities as well as open circuit voltages (OCV) at 700 and 800 °C. Experimental results are presented in Table 5.2. As mentioned in the previous section, higher operation temperature resulted in lower OCV due to the increase in the electronic conductivity of SDC electrolytes. Comparison of open circuit voltages between fuel cells fabricated using SDC electrolytes made with pre sintering powders (table 5.1) and fuel cells fabricated with electrolytes made using only fresh powders (table 5.2) revealed a decrease on the experimental OCV when using pre sintered electrolytes. Similarly, examination of maximum powder densities (figure 5.1 and 5.2) evidenced a significant performance difference. SOFCs fabricated using fresh SDC powders achieved higher power densities than the respective fuel cells made using pre sintered SDC powders.

Inspection of the fuel cell overall internal resistance (as determined by the slope of the *VI* curve) evidenced a higher resistance from fuel cells fabricated with pre sintered SDC powders. Analysis of the performance obtained from both types of fuel cells motivated an additional analysis on the electrolyte layers, as discussed in section 5.3.

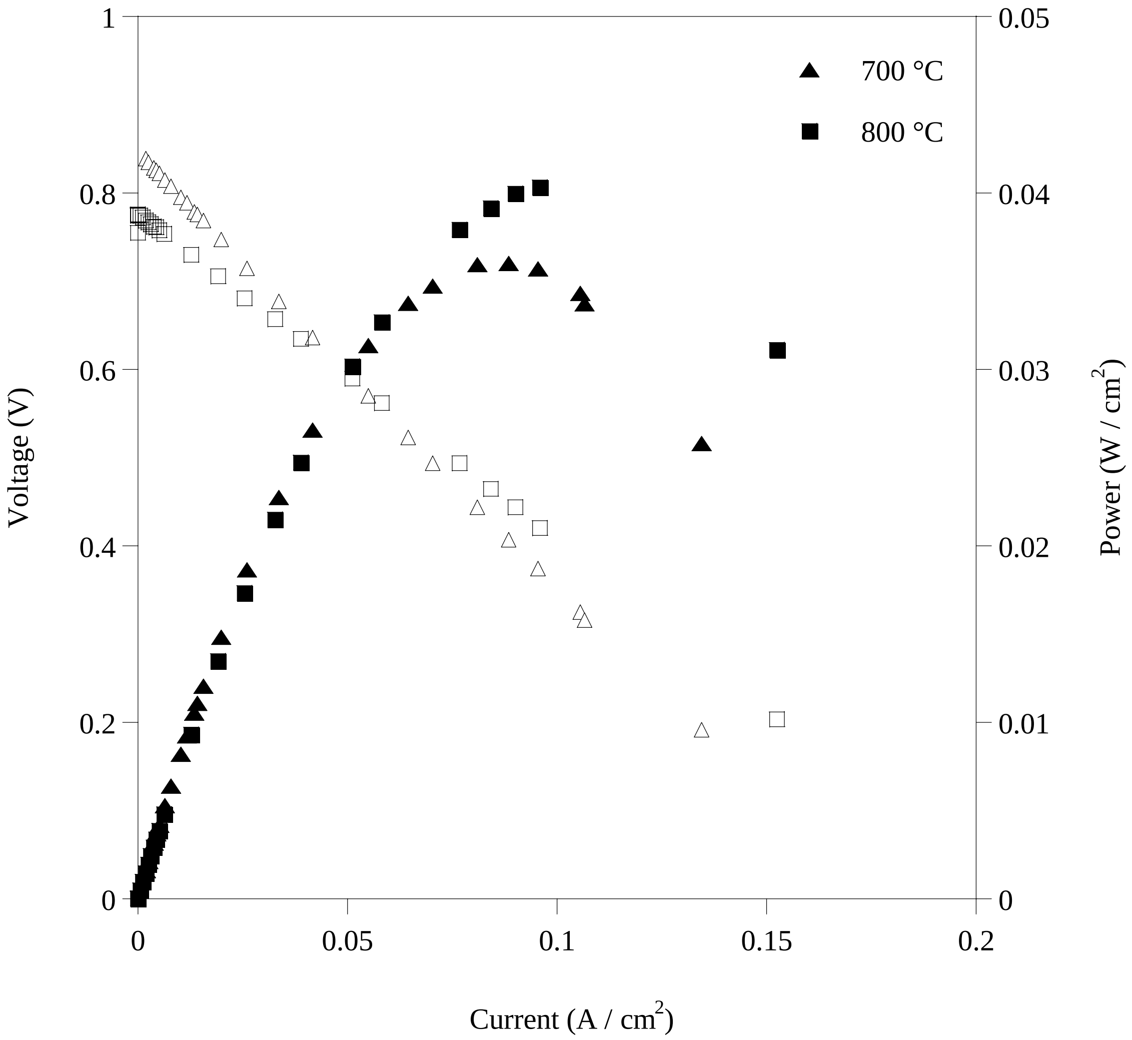

Figure 5.2 *V-I* curves (open symbols) and their corresponding power densities at 700, and 800 °C for an electrolyte supported cell fabricated by mixing pre sintered and fresh SDC powders as described in section 4.3.2.2.

Table 5.2 Open circuit voltage (OCV) and maximum power density for fuel cells fabricated using pre sintered SDC powders.

Operating temperature (°C)	**OCV (Volt)**	**Max Power density (W/cm2)**
700	0.841	0.0361
800	0.783	0.0409

5.3 Influence of electrolyte preparation on fuel cell performance.

Comparison of *VI* curves obtained from fuel cells fabricated using mixtures of pre-sintered SDC powders and fuel cells made exclusively with fresh SDC evidenced the impact of fabrication procedures on the fuel cell performance. Considering that the operation of fuel cells requires that the O^{-2} ions produced in the cathode active sites diffuse consecutively through the bulk of the cathode electrode, the electrolyte, and the bulk of the anode electrode until reaching the anode sites in order to react with the fuel, the performance of the fuel cell will be limited by the individual resistance of each successive layers (cathode electrode, electrolyte, and anode electrode). Detailed evaluation of individual resistance of the electrodes and electrolytes requires the use of special characterization techniques such as impedance spectroscopy, which was not available in the course of study. However it is reasonable to believe that the difference in the resistance of these two types of fuel cells comes from the electrolyte material, since the electrodes were fabricated according to the same procedure.

As mentioned in section 2.3 the ion transport of fluorite structure solid electrolytes occurs by successive jumping of charged species through adjacent oxygen vacancies. Equation 2.5 shows that ionic conductivity is proportional to the jumping distance separating two oxygen vacancies, therefore electrolyte materials having low resistance are usually very dense (no empty space between particles). Motivated by this thought, SEM micrographs were taken to the SDC electrolyte layers made with pre sintered powders and to those SDC layers made with fresh powders. Results revealed the presence of small pores in the SDC electrolyte layers of the former. Figure 5.3 present SEM micrographs fro the SDC electrolytes made using pre sintered powders and fresh (not heat treated) powders.

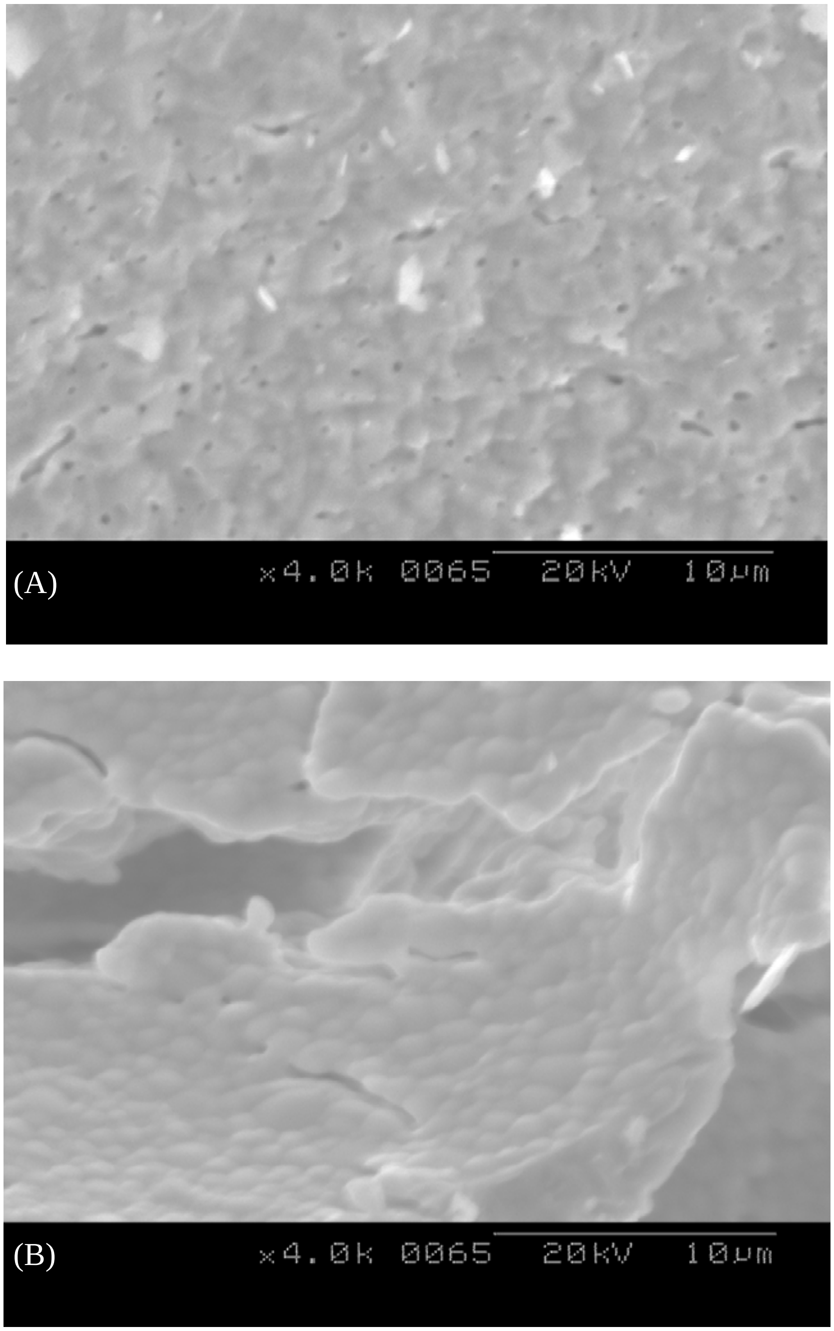

Figure 5.3 SEM micrographs presenting (A) Small pores on SDC electrolytes made with pre sintered powders and (B) Fractured SDC electrolyte layers fabricated using only fresh powders.

CHAPTER VI

CONCLUSION

The objectives proposed in this study consisted on investigating the synthesis of fuel cell materials such as samarium doped ceria (SDC) electrolytes and strontium doped samarium cobaltite (SSC) electrodes, their utilization in the fabrication of intermediate temperature solid oxide fuel cells (IT-SOFCs) and the evaluation of operation conditions maximizing their fuel cell power density. Results obtained during this study evidenced that SDC electrolyte materials having fluorite structure and SSC electrode materials having perovskite structure can be successfully synthesized according to the proposed pechini method and solid state reaction, as evidenced by different characterization techniques such as X-ray diffractometry, Raman spectroscopy and scanning electron microscopy. Electrolyte supported IT-SOFCs successfully were fabricated using an SDC electrolyte material and an SSC anode and cathode electrode by the cold pressing technique. Additives such as Binders, dispersants, and solvents as well as their specific concentrations were found to have a profound impact on the physical properties of electrolyte and electrode layers, affecting the performance of the resulting fuel cells. Densification of SDC electrolyte layers was found sensitive to specific heat treatments during its fabrication. The use of mixtures of SDC electrolyte powders (pre-sintered and fresh) was found to have a detrimental effect during the densification of electrolyte layers. Fuel cell maximum power density and internal resistance was evaluated at different operation temperatures. Results indicated a dependence of maximum power density of fabricated fuel cells on the characteristics of the electrolyte material. Particularly, the electrolyte density was found to have a profound effect on the performance on the fuel cell. Finally, the use of SSC perovskite materials acting as anode and cathode electrode in a single cell (eliminating an intermediate firing step) was successfully implemented.

Future work would be directed towards the development of higher performance SSC / SDC /SSC solid oxide fuel cells. Studies focusing on the development of higher performance anode electrodes capable of processing different gaseous fuels (i.e. hydrocarbons) as well as Carbon will be preformed. Introduction of different promoting metal catalysts such as Ag and Cu on SSC anode electrodes will be tested under different operation conditions. Introduction of Carbon pore formers into the SSC electrodes during the fabrication stage and their effect on the electrode layer surface area will be studied. Evaluation of the SSC electrode long term stability under strong reducing environments will also be evaluated. Finally, different fuel cell architectures such as anode and cathode supported fuel cells will be evaluated in order to enhance the oxygen ion transport of the fuel cell and thus enhancing the fuel cell performance.

BIBLIOGRAPHY

CHAPTER I:

1. IEA, “World Energy Outlook” (DOE/EIA-0484(2004), 2004).

2. F. Birol, M. Argiri, *Energy (Oxford)* **24**, 905 (1999).

3. A. B. Stambouli, E. Traversa, *Renewable & Sustainable Energy Reviews* **6**, 433 (2002).

4. IEA, “World energy Outlook” (1998).

5. A. J. Cavallo, *Natural Resources Research (Dordrecht, Netherlands)* **13**, 211 (2004).

6. E. Stokstad, *Science (Washington, DC, United States)* **308**, 1530 (2005).

7. D. A. Stainforth *et al.*, *Nature (London, United Kingdom)* **433**, 403 (2005).

8. Z. Pan, M. Segal, R. W. Arritt, E. S. Takle, *Renewable Energy* **29**, 1923 (2004).

9. R. Agrawal, M. Offutt, M. P. Ramage, *AIChE Journal* **51**, 1582 (2005).

10. L. Barreto, A. Makihira, K. Riahi, *International Journal of Hydrogen Energy* **28**, 267 (2002).

11. J. O. M. Bockris, *International Journal of Hydrogen Energy* **27**, 731 (2002).

12. M. Conte, A. Iacobazzi, M. Ronchetti, R. Vellone, *Journal of Power Sources* **100**, 171 (2001).

13. M. G. Schultz, T. Diehl, G. P. Brasseur, W. Zittel, *Science (Washington, DC, United States)* **302**, 624 (2003).

14. G. W. Crabtree, M. S. Dresselhaus, M. V. Buchanan, *Physics Today* **57**, 39 (2004).

15. D. M. Kammen, T. E. Lipman, *Science (Washington, DC, United States)* **302**, 226 (2003).

16. F. Kreith, R. West, *Journal of Energy Resources Technology* **126**, 249 (2004).

17. R. Moy, *Science (Washington, DC, United States)* **301**, 47 (2003).

18. S. A. Sherif, F. Barbir, T. N. Veziroglu, *Solar Energy* **78**, 647 (2005).

19. D. A. J. Rand, R. M. Dell, *Journal of Power Sources* **144**, 568 (2005).

20. W. Vielstich, *Fuel Cells; Modern Processes for the Electrochemical Production of Energy* (1970), pp. 501 pp.

21. E. G. T. services, “Fuel cell Handbook” (DOE, 2002).

22. N. Q. Minh, *Solid State Ionics* **174**, 271 (2004).

23. S. P. S. Badwal, *Solid State Ionics* **143**, 39 (2001).

24. T. Matsui, T. Kosaka, M. Inaba, A. Mineshige, Z. Ogumi, *Solid State Ionics* **176**, 663 (2005).

25. Y. Liu, S. Zha, M. Liu, *Advanced Materials (Weinheim, Germany)* **16**, 256 (2004).

26. C. Xia, W. Rauch, F. Chen, M. Liu, *Solid State Ionics* **149**, 11 (2002).

27. Y. Liu, W. Rauch, S. Zha, M. Liu, *Solid State Ionics* **166**, 261 (2004).

CHAPTER II:

1. S. P. S. Badwal, *Solid State Ionics* **143**, 39 (2001).

2. C. Xia, W. Rauch, F. Chen, M. Liu, *Solid State Ionics* **149**, 11 (2002).

3. S. C. Singhal, *Solid State Ionics* **135**, 305 (2000).

4. V. V. Kharton, F. M. B. Marques, A. Atkinson, *Solid State Ionics* **174**, 135 (2004).

5. S. C. Singhal, K. Kendall, *High Temperature Solid Oxide Fuel Cell : Fundamentals, Design and Applications* (2003), pp. 405.

6. S. V. Kesapragada, S. B. Bhaduri, S. Bhaduri, P. Singh, *Journal of Power Sources* **124**, 499 (2003).

7. P. R. Slater, J. E. H. Sansom, J. R. Tolchard, *Chemical Record* **4**, 373 (2005).

8. M. F. Lasker, R. A. Rapp, *Zeitschrift fuer Physikalische Chemie (Muenchen, Germany)* **49**, 198 (1966).

9. J. M. Wimmer, L. R. Bidwell, N. M. Tallan, *Journal of the American Ceramic Society* **50**, 198 (1967).

10. R. N. Blumenthal, J. E. Garnier, *Journal of Solid State Chemistry* **16**, 21 (1976).

11. H. Inaba, H. Tagawa, *Solid State Ionics* **83**, 1 (1996).

12. J. M. Dixon, L. D. LaGrange, U. Merten, C. F. Miller, J. T. Porter, II, *Journal of the Electrochemical Society* **110**, 276 (1963).

13. D. W. Strickler, W. G. Carlson, *Journal of the American Ceramic Society* **48**, 286 (1965).

14. H. A. Johansen, J. G. Cleary, *Journal of the Electrochemical Society* **111**, 100 (1964).

15. T. Takahashi, T. Esaka, H. Iwahara, *Journal of Applied Electrochemistry* **7**, 299 (1977).

16. N. M. Sammes, G. A. Tompsett, H. Nafe, F. Aldinger, *Journal of the European Ceramic Society* **19**, 1801 (1999).

17. T. Takahashi, H. Iwahara, T. Arao, *Journal of Applied Electrochemistry* **5**, 187 (1975).

18. T. Takahashi, H. Iwahara, Y. Nagai, *Journal of Applied Electrochemistry* **2**, 97 (1972).

19. T. Takahashi, H. Iwahara, *Journal of Applied Electrochemistry* **3**, 65 (1973).

20. S. Skinner, J. Kilner, *Materials Today (Oxford, United Kingdom)* **6**, 30 (2003).

21. J. C. Boivin, G. Mairesse, *Chemistry of Materials* **10**, 2870 (1998).

22. X. Zhang *et al.*, *Solid State Ionics* **133**, 153 (2000).

23. A. Endo, M. Ihara, H. Komiyama, K. Yamada, *Solid State Ionics* **86-88**, 1191 (1996).

24. H. Yahiro, T. Ohuchi, K. Eguchi, H. Arai, *Journal of Materials Science* **23**, 1036 (1988).

25. H. Yahiro, K. Eguchi, H. Arai, *Solid State Ionics* **36**, 71 (1989).

26. H. L. Tuller, A. S. Nowick, *Journal of the Electrochemical Society* **122**, 255 (1975).

27. R. N. Blumenthal, B. A. Pinz, *Journal of Applied Physics* **38**, 2376 (1967).

28. T. Takahashi, K. Ito, H. Iwahara, *Revue Energie Primaire* **2**, 42 (1966).

29. N. Maffei, A. K. Kuriakose, *Journal of Power Sources* **75**, 162 (1998).

30. M. Feng, J. B. Goodenough, K. Huang, C. Milliken, *Journal of Power Sources* **63**, 47 (1996).

31. F. Chen, M. Liu, *Journal of Solid State Electrochemistry* **3**, 7 (1998).

32. S. Sameshima, T. Ichikawa, M. Kawaminami, Y. Hirata, *Materials Chemistry and Physics* **61**, 31 (1999).

33. W. Huang, P. Shuk, M. Greenblatt, *Chemistry of Materials* **9**, 2240 (1997).

34. I. P. Marozau *et al.*, *Materials Research Bulletin* **40**, 361 (2005).

35. G. C. Kostogloudis, C. Ftikos, *Journal of the European Ceramic Society* **18**, 1711 (1998).

36. V. V. Kharton, E. N. Naumovich, A. A. Yaremchenko, F. M. B. Marques, *Journal of Solid State Electrochemistry* **5**, 160 (2001).

37. T. Mori, J. Drennan, J.-H. Lee, J.-G. Li, T. Ikegami, *Solid State Ionics* **154-155**, 461 (2002).

38. D. Hirabayashi, A. Tomita, S. Teranishi, T. Hibino, M. Sano, *Solid State Ionics* **176**, 881 (2005).

39. V. V. Kharton, A. A. Yaremchenko, E. N. Naumovich, F. M. B. Marques, *Journal of Solid State Electrochemistry* **4**, 243 (2000).

40. T. Matsui, T. Kosaka, M. Inaba, A. Mineshige, Z. Ogumi, *Solid State Ionics* **176**, 663 (2005).

41. T. Mori *et al.*, *Solid State Ionics* **175**, 641 (2004).

42. S. Tao, J. T. S. Irvine, *Chemical Record* **4**, 83 (2004).

43. W. Z. Zhu, S. C. Deevi, *Materials Science & Engineering, A: Structural Materials: Properties, Microstructure and Processing* **A362**, 228 (2003).

44. S. P. Jiang, S. H. Chan, *Journal of Materials Science* **39**, 4405 (2004).

45. S. P. Jiang, S. P. S. Badwal, *Journal of the Electrochemical Society* **144**, 3777 (1997).

46. H. Uchida, M. Yoshida, M. Watanabe, *Journal of Physical Chemistry* **99**, 3282 (1995).

47. M. Mori, T. Yamamoto, H. Itoh, H. Inaba, H. Tagawa, *Journal of the Electrochemical Society* **145**, 1374 (1998).

48. T. Setoguchi, K. Okamoto, K. Eguchi, H. Arai, *Journal of the Electrochemical Society* **139**, 2875 (1992).

49. B. C. H. Steele, I. Kelly, H. Middleton, R. Rudkin, *Solid State Ionics* **28-30**, 1547 (1988).

50. A. L. Dicks, *Journal of Power Sources* **61**, 113 (1996).

51. J.-H. Koh, Y.-S. Yoo, J.-W. Park, H. C. Lim, *Solid State Ionics* **149**, 157 (2002).

52. R. J. Gorte, S. Park, J. M. Vohs, C. Wang, *Advanced Materials (Weinheim, Germany)* **12**, 1465 (2000).

53. S. McIntosh, J. M. Vohs, R. J. Gorte, *Journal of the Electrochemical Society* **150**, A470 (2003).

54. S. Park, J. M. Vohs, R. J. Gorte, *Nature (London)* **404**, 265 (2000).

55. H. Kim, C. Lu, W. L. Worrell, J. M. Vohs, R. J. Gorte, *Journal of the Electrochemical Society* **149**, A247 (2002).

56. S. Primdahl, J. R. Hansen, L. Grahl-Madsen, P. H. Larsen, *Journal of the Electrochemical Society* **148**, A74 (2001).

57. G. Pudmich *et al.*, *Solid State Ionics* **135**, 433 (2000).

58. J. Canales-Vazquez, S. W. Tao, J. T. S. Irvine, *Solid State Ionics* **159**, 159 (2003).

59. S. Hui, A. Petric, *Journal of the Electrochemical Society* **149**, J1 (2002).

60. S. Hui, A. Petric, *Journal of the European Ceramic Society* **22**, 1673 (2002).

61. A. Hartley, M. Sahibzada, M. Weston, I. S. Metcalfe, D. Mantzavinos, *Catalysis Today* **55**, 197 (2000).

62. Y. Takeda *et al.*, *Solid State Ionics* **72**, 257 (1994).

63. A. V. Berenov, J. L. MacManus-Driscoll, J. A. Kilner, *Solid State Ionics* **122**, 41 (1999).

64. J. Van Herle, A. J. McEvoy, K. R. Thampi, *Electrochimica Acta* **41**, 1447 (1996).

65. T. Kawada *et al.*, *Solid State Ionics* **121**, 271 (1999).

66. H. Y. Tu, Y. Takeda, N. Imanishi, O. Yamamoto, *Solid State Ionics* **100**, 283 (1997).

67. M. Goedickemeier, K. Sasaki, L. J. Gauckler, I. Riess, *Solid State Ionics* **86-88**, 691 (1996).

68. A. Mineshige *et al.*, *Journal of Solid State Chemistry* **142**, 374 (1999).

69. Y. Takeda *et al.*, *Solid State Ionics* **86-88**, 1187 (1996).

70. T. Hibino *et al.*, *Science (Washington, D. C.)* **288**, 2031 (2000).

71. A. B. Stambouli, E. Traversa, *Renewable & Sustainable Energy Reviews* **6**, 433 (2002).

72. K. Yamashita, K. V. Ramanujachary, M. Greenblatt, *Solid State Ionics* **81**, 53 (1995).

73. J. A Kilner, B. C. H Steele, Nonstoichiom. Oxides 233 (1981).

CHAPTER IV:

1. H. Nitani *et al.*, *Materials Letters* **58**, 2076 (2004).

2. R. Peng, C. Xia, D. Peng, G. Meng, *Materials Letters* **58**, 604 (2004).

3. J.-G. Li, T. Ikegami, T. Mori, *Acta Materialia* **52**, 2221 (2004).

4. D. Y. Chung, E. H. Lee, *Journal of Alloys and Compounds* **374**, 69 (2004).

5. K. Yamashita, K. V. Ramanujachary, M. Greenblatt, *Solid State Ionics* **81**, 53 (1995)

6. F.-Y. Wang, S. Chen, S. Cheng, *Electrochemistry Communications* **6**, 743 (2004).

7. J. P. Hos, P. G. McCormick, *Scripta Materialia* **48**, 85 (2003).

8. F.-Y. Wang, B.-Z. Wan, S. Cheng, *Journal of Solid State Electrochemistry* **9**, 168 (2005).

9. S. Zhao, R. J. Gorte, *Applied Catalysis, A: General* **248**, 9 (2003).

10. J.-G. Li, T. Ikegami, T. Mori, T. Wada, *Chemistry of Materials* **13**, 2921 (2001).

11. T. Shimonosono *et al.*, *Solid State Ionics* **174**, 27 (2004).

12. W. H. Weber, K. C. Hass, J. R. McBride, *Physical Review B: Condensed Matter and Materials Physics* **48**, 178 (1993).

13. A. Mineshige *et al.*, *Solid State Ionics* **135**, 481 (2000).

14. J. R. McBride, K. C. Hass, B. D. Poindexter, W. H. Weber, *Journal of Applied Physics* **76**, 2435 (1994).

15. S. Wang, T. Chen, S. Chen, *Journal of the Electrochemical Society* **151**, A1461 (2004).

16. K. Higashi, K. Sonoda, H. Ono, S. Sameshima, Y. Hirata, *Journal of Materials Research* **14**, 957 (1999).

17. J. P. Hos, P. G. McCormick, *Journal of the Australasian Ceramic Society* **38**, 139 (2002).

18. E. M. Anderson, R. A. Marra, R. E. Mistier, *American Ceramic Society Bulletin* **76**, 45 (1997).

19. Y. J. Leng, S. H. Chan, K. A. Khor, S. P. Jiang, P. Cheang, *Journal of Power Sources* **117**, 26 (2003).

20. G. B. Jung, T. J. Huang, M. H. Huang, C. L. Chang, *Journal of Materials Science* **36**, 5839 (2001).

21. J. Van Herle *et al.*, *Solid State Ionics* **86-88**, 1255 (1996).

22. I. Riess, D. Braunshtein, D. S. Tannhauser, *Journal of the American Ceramic Society* **64**, 479 (1981).

23. T. Kudo, H. Obayashi, *Journal of the Electrochemical Society* **122**, 142 (1975).

24. Y. S. Zhen, S. J. Milne, R. J. Brook, *Science of Ceramics* **14**, 1025 (1988).

25. K. Huang, M. Feng, J. B. Goodenough, *Journal of the American Ceramic Society* **81**, 357 (1998).

26. S. Nakane, T. Tachi, M. Yoshinaka, K. Hirota, O. Yamaguchi, *Journal of the American Ceramic Society* **80**, 3221 (1997).

27. Y. Zhou, R. J. Phillips, J. A. Switzer, *Journal of the American Ceramic Society* **78**, 981 (1995).

28. W. Huang, P. Shuk, M. Greenblatt, *Chemistry of Materials* **9**, 2240 (1997).

29. F. F. Lange, *Journal of the American Ceramic Society* **67**, 83 (1984).

30. W. D. Kingery, B. Francois, *Sintering Relat. Phenomena, Proc. Int. Conf., 2nd,* 471 (1967).

31. R. K. McGeary, *Journal of the American Ceramic Society* **44**, 513 (1961).

32. C. Xia, W. Rauch, F. Chen, M. Liu, *Solid State Ionics* **149**, 11 (2002).

33. T. Hibino *et al.*, *Science (Washington, D. C.)* **288**, 2031 (2000).

CHAPTER V:

1. T. Matsui, T. Kosaka, M. Inaba, A. Mineshige, Z. Ogumi, *Solid State Ionics* **176**, 663 (2005).

2. C. Xia, W. Rauch, F. Chen, M. Liu, *Solid State Ionics* **149**, 11 (2002).

3. H. Inaba, H. Tagawa, *Solid State Ionics* **83**, 1 (1996).

4. T. Mori, J. Drennan, J.-H. Lee, J.-G. Li, T. Ikegami, *Solid State Ionics* **154-155**, 461 (2002).

5. D. Hirabayashi, A. Tomita, S. Teranishi, T. Hibino, M. Sano, *Solid State Ionics* **176**, 881 (2005).

6. M. Price *et al.*, *Journal of the American Ceramic Society* **88**, 1812 (2005).

APPENDIX:

1. W. Vielstich, Fuel Cells; Modern Processes for the Electrochemical Production of Energy (1970), pp. 501 pp.

2. G. Aragon-Gonzalez, A. Canales-Palma, A. Leon-Galicia, M. Musharrafie-Martinez, Journal of Physics D: Applied Physics 36, 280 (2003).

3. N. J. Cherepy, R. Krueger, K. J. Fiet, A. F. Jankowski, J. F. Cooper, Journal of the Electrochemical Society 152, A80 (2005).

4. S. P. S. Badwal, K. Foger, Ceramics International 22, 257 (1996).

APPENDIX

FUEL CELL EFFICIENCY

Thermodynamic analysis of heat engines can be used to show that the efficiency of fuel cells exceeds that of conventional energy conversion technologies (i.e. internal combustion engines) by considering the thermal efficiency of an ideal reversible heat engine (i.e. Carnot engine) operating between two systems held at different temperatures (T_1, T_2, $T_1 > T_2$). The efficiency of such heat engine can be defined as the ratio of the maximum work that can be obtained to the heat supplied from the hot system held at T_1, as shown in the following equation.

$$\eta = \frac{work\ output}{heat\ input} = -\frac{W_{\max}}{Q_1}$$

Evaluation of the energy balance around the heat engine allows expressing the efficiency of the heat engine as

$$\eta = -\frac{W_{\max}}{Q_1} = \frac{Q_1 + Q_2}{Q_1} = 1 + \frac{Q_2}{Q_1}$$

Taking into account that for such ideally reversible processes are considered isentropic the following relation follows.

$$\Delta \mathrm{S} = \frac{\mathrm{Q}_1}{\mathrm{T}_1} + \frac{\mathrm{Q}_2}{\mathrm{T}_2} = 0$$

$$-\frac{\mathrm{Q}_2}{\mathrm{Q}_1} = \frac{\mathrm{T}_2}{\mathrm{T}_1}$$

As a result the efficiency of a heat engine can be expressed according to the Carnot equation (*1*).

$$\eta = \frac{W_{\max}}{Q_1} = 1 + \frac{Q_2}{Q_1} = 1 - \frac{T_2}{T_1} = \frac{T_1 - T_2}{T_1}$$

$$W_{\max} = Q_1 \cdot \frac{T_1 - T_2}{T_1}$$

When the heat transferred at the higher temperature comes from a combustion reaction, Q_1 can be identified as the heat released (-ΔH) from the reaction. Therefore it is clear that the only alternative to achieve a 100% efficiency requires that $T_2 = 0$ K. In practical applications the optimum efficiency of power stations is between 20 to 40 % (*2*).

In contrast to thermoelectric energy converters, fuel cells can achieve theoretical efficiencies of 100% or more with respect to the heat of reaction -ΔH (*1, 3, 4*). The maximum amount of energy that can be drawn as work from a chemical reaction is determined by the Gibbs free energy (*4*).

$$\Delta \mathrm{G} = \Delta \mathrm{H} - \mathrm{T}\Delta \mathrm{S}$$

Where ΔH and ΔS are the enthalpy and entropy of reaction at the absolute temperature T (Only reactions having $\Delta G < 0$ are capable of providing a positive amount of work for external utilization). The maximum electrical work obtainable from an energy producing reaction by means of an electrochemical device is related to the Gibbs free energy of the cell reaction.

$$\Delta G = nFE$$

Where E is the electromotive force of the cell (emf), F is the Faraday constant (96493 coul/g equiv), and n is the number of electrons transferred in the course of the electrochemical reaction of the cell. The negative sign indicates that a positive amount of electrical energy is obtained from the Gibbs energy loss due to the reaction. If all reactants and products are in standard states the emf of the cell becomes the standard emf, $E°$, which is similarly related to the standard Gibbs free energy of reaction by:

$$\Delta G^{\circ} = nFE^{\circ}$$

The dependence of the emf on pressure as well as in temperature has been studied by inspecting the dependence of the Gibbs free energy with respect to pressure at constant temperature.

$$\left(\frac{\partial G}{\partial P}\right)_T = \Delta V$$

If ideal gas behavior can be assumed, such as in the case of a H_2 fuel cell, the volume of each gas and change of volume during the reactions can be expressed as

$$V = \frac{RT}{P}$$
$$\Delta V = \sum_i \nu_i RT / P$$

Where ν_i represent the stoichiometric coefficients of the gaseous reacting species (positive fro products, negative for reactants). From this expression it is possible to express the Gibbs free energy of reaction as shown in the following equation

$$\Delta G = \Delta G^\circ + \sum_i \nu_i RT \ln p_i / p_i^\circ$$

Similarly, the emf of the cell of the cell in which the reaction proceeds with gaseous species at non-standard pressures can be expressed as

$$\Delta E = \Delta E^\circ - \frac{RT}{nF} \sum_i \nu_i \ln p_i / p_i^\circ$$

This equation can be used in order to calculate the theoretical emf of the fuel cell.

Under experimental conditions the efficiency of a fuel cell depends on a great number of factors including, the type of fuel feed to the system, the operating temperature and pressure, the specific characteristics of the electrolyte and electrodes, and the specific architecture of the fuel cell. However, the thermodynamic efficiency of a fuel cell (η_{FC}) can be easily evaluated by analyzing the electrochemical reactions.

$$\eta_{FC} = \frac{\Delta G}{\Delta H} = \frac{\Delta H - T\Delta S}{\Delta H} = 1 - T\frac{\Delta S}{\Delta H}$$

Depending on the nature of the reaction under study the maximum achievable efficiency varies. For electrochemical reactions involving no change in the number of gas moles, ΔS is close to zero and the ideal efficiency becomes η_{FC} =100%.